

Seeing the Outer Edge of the Infant Type Ia Supernova 2024epr in the Optical and Near Infrared

W. B. HOOGENDAM^{1*}, D. O. JONES², C. ASHALL¹, B. J. SHAPPEE¹, R. J. FOLEY³, M. A. TUCKER^{4,5,†}, M. E. HUBER¹, K. AUCHETTL^{6,3}, D. D. DESAI¹, A. DO^{7,8}, J. T. HINKLE^{1‡}, S. ROMAGNOLI⁶, J. SHI⁶, A. SYNCATTO^{1,9}, C. R. ANGUS^{10,11}, K. C. CHAMBERS¹, D. A. COULTER¹², K. W. DAVIS³, T. DE BOER¹, A. GAGLIANO^{13,14}, M. Y. KONG¹, C.-C. LIN¹, T. B. LOWE¹, E. A. MAGNIER¹, P. MÍNGUEZ¹, Y.-C. PAN¹⁵, K.C. PATRA³, S. A. SEVERSON¹⁶, K. TAGGART³, A. R. WASSERMAN^{17,18}, S. K. YADAVALLI¹³, P. CHEN^{19,20}, AND R. S. POST²¹

¹Institute for Astronomy, University of Hawai'i, Honolulu, HI 96822, USA

²Institute for Astronomy, University of Hawai'i, 640 N. A'ohoku Pl., Hilo, HI 96720, USA

³Department of Astronomy and Astrophysics, University of California, Santa Cruz, CA 95065, USA

⁴Center for Cosmology & Astroparticle Physics, The Ohio State University, Columbus, OH, USA

⁵Department of Astronomy, The Ohio State University, Columbus, OH, USA

⁶School of Physics, University of Melbourne, Parkville, VIC 3010, Australia

⁷Institute of Astronomy, Cambridge, CB3 0HA, UK

⁸Kavli Institute for Cosmology, Cambridge, CB3 0HA, UK

⁹Department of Physics & Astronomy, University of Hawai'i at Hilo, Hilo, HI 96720, USA

¹⁰Astrophysics Research Centre, School of Mathematics and Physics, Queen's University Belfast, Belfast BT7 1NN, UK

¹¹DARK, Niels Bohr Institute, University of Copenhagen, Jagtvej 128, DK-2200 Copenhagen Ø Denmark

¹²Space Telescope Science Institute, Baltimore, MD 21218, USA

¹³Center for Astrophysics | Harvard & Smithsonian, Cambridge, MA 02138, USA

¹⁴The NSF AI Institute for Artificial Intelligence and Fundamental Interactions

¹⁵Graduate Institute of Astronomy, National Central University, 300 Zhongda Road, Zhongli, Taoyuan 32001, Taiwan

¹⁶Department of Physics & Astronomy, Sonoma State University, Rohnert Park, CA 94928, USA

¹⁷Department of Astronomy, University of Illinois at Urbana-Champaign, Urbana, IL 61801, USA

¹⁸Center for Astrophysical Surveys, National Center for Supercomputing Applications, Urbana, IL 61801, USA

¹⁹Institute for Advanced Study in Physics, Zhejiang University, Hangzhou 310027, China

²⁰Institute for Astronomy, School of Physics, Zhejiang University, Hangzhou 310027, China and

²¹Post Astronomy, Lexington, MA 02421

Version August 20, 2025

ABSTRACT

We present optical-to-near-infrared (NIR) photometry and spectroscopy of the Type Ia supernova (SN Ia) 2024epr, including NIR spectra observed within two days of first light. The early-time optical spectra show strong, high-velocity Ca and Si features near rarely-observed velocities at $\sim 0.1c$, and the NIR spectra show a C I “knee.” Despite early-time, high-velocity features, SN 2024epr evolves into a normal SN Ia, albeit with stronger peak-light Ca absorption than other SNe Ia with the same light curve shape. Although we infer a normal decline rate, $\Delta m_{15}(B) = 1.09 \pm 0.12$ mag, from the light-curve rise, SN 2024epr is a Branch “cool” object and has red early-time colors ($g-r \approx 0.15$ mag at -10 days). The high velocities point to a density enhancement in the outer layers of the explosion, predicted by some models, but thick-shell He-detonation models do not match the smoothly rising light curve or apparent lack of He in our early-time NIR spectra. No current models (e.g., delayed detonation or thin He shell double detonation) appear to reproduce all observed properties, particularly the unusual early-time colors. Such constraints are only possible for SN 2024epr from the earliest optical and NIR observations, highlighting their importance for constraining SN Ia models. Finally, we identify several literature SNe Ia with intermediate mass elements at $\sim 30\,000$ km s $^{-1}$ within days after the explosion that evolve into otherwise normal SNe Ia at peak light, suggesting the early-time spectra of SNe Ia may hide a broad diversity of observational characteristics.

Subject headings: Type Ia supernovae(1728) — Optical astronomy(1776) — Near-infrared astronomy(1093)

1. INTRODUCTION

Type Ia supernovae (SNe Ia) are oft-occurring (e.g., Desai et al. 2024) astronomical transients associated with the thermonuclear explosions of carbon-oxygen white dwarf stars (CO WDs; Hoyle & Fowler 1960). They produce a significant fraction of the intermediate mass and Fe-group elements in the Universe (e.g., Raiteri et al.

1996; Matteucci & Recchi 2001) and enable precise distance determinations (Phillips 1993) useful for constraining cosmological parameters (Riess et al. 1998; Perlmutter et al. 1999; Burns et al. 2018; Jones et al. 2022; Riess et al. 2022). Despite the many SN Ia data sets (e.g., Hicken et al. 2009; Ganeshalingam et al. 2010; Brown et al. 2014; Krisciunas et al. 2017; Holoi et al. 2017a,b,c; Foley et al. 2018; Holoi et al. 2019; Jones et al. 2019; Phillips et al. 2019; Tucker et al. 2020; Fausnaugh et al. 2021; Jones et al. 2021; Scolnic et al. 2022; Fausnaugh et al. 2023; Neumann et al. 2023; Peterson

*NSF Fellow

†CCAPP Fellow

‡FINESST Fellow

Corresponding author: willemh@hawaii.edu

et al. 2023; Morrell et al. 2024; Do et al. 2025) and theoretical models (e.g., Nomoto et al. 1984; Thielemann et al. 1986; Khokhlov 1991; Woosley & Weaver 1994; Hoeflich et al. 1995; Hoeflich & Khokhlov 1996; Iwamoto et al. 1999; Röpke & Niemeyer 2007; Shen et al. 2010; Woosley & Kasen 2011; Pakmor et al. 2012; Seitenzahl et al. 2013; Fink et al. 2014), the progenitor systems and explosion mechanisms of SNe Ia are not yet fully understood, and fundamental, qualitative questions remain unanswered (reviews include Maoz et al. 2014; Jha et al. 2019; Liu et al. 2023).

While there is broad consensus and strong evidence (Hoyle & Fowler 1960; Nugent et al. 2011) that SNe Ia originate from exploding CO WDs, many disparate models exist. Each model includes a progenitor scenario (i.e., the constituent objects before any explosion occurs) and an explosion mechanism (i.e., how the CO WD ignites thermonuclear runaway). Two oft-invoked progenitor scenarios are the single-degenerate (SD) scenario with a CO WD and a non-degenerate companion such as a main sequence or red giant star (e.g., Whelan & Iben 1973; Nomoto 1982b; Nomoto et al. 1997) and the double-degenerate (DD) scenario with at least two CO WDs or a CO WD and a He WD (e.g., Nomoto 1980; Iben & Tutukov 1984; Webbink 1984). Other scenarios exist as well, such as the core-degenerate (CD) scenario involving a CO WD and the degenerate CO core of an asymptotic giant branch star (AGB star; e.g., Hoeflich & Khokhlov 1996), but are most often invoked only to explain highly peculiar SNe Ia (e.g., 2003fg-like SNe Ia Lu et al. 2021; Ashall et al. 2021).

As with the progenitor scenario, several explosion mechanisms may produce a SN Ia. Historically, SNe Ia were thought to detonate (i.e., explode with a supersonic propagation speed) when they near the Chandrasekhar mass ($M_{\text{ch}} \approx 1.4 M_{\odot}$, Chandrasekhar 1931). However, subsequent studies have found different explosion mechanisms may produce SNe Ia below, at, or above this mass. For example, material from either a degenerate (DD scenario) or non-degenerate (SD scenario) companion can accrete onto the CO WD, triggering an explosion through central carbon ignition as the CO WD approaches the Chandrasekhar mass (Hoyle & Fowler 1960; Whelan & Iben 1973; Nomoto 1982a; Piersanti et al. 2003) or through a He detonation on the surface of a CO WD below the Chandrasekhar mass (Nomoto 1980, 1982b; Livne 1990; Woosley & Weaver 1994; Hoeflich & Khokhlov 1996; Shen & Moore 2014; Hoeflich et al. 2017; Maeda et al. 2018; Shen et al. 2018; Polin et al. 2019; Gronow et al. 2020; Shen et al. 2024). Alternatively, a merger (Iben & Tutukov 1984; Webbink 1984; van Kerkwijk et al. 2010; Scalzo et al. 2010; Pakmor et al. 2010, 2013; Kromer et al. 2013, 2016; Tucker 2025) or a third/fourth-body induced collision of two CO WDs (Rosswog et al. 2009; Raskin et al. 2009; Thompson 2011; Kushnir et al. 2013; Pejcha et al. 2013) may occur in the DD scenario causing explosions with a wide range of masses less than, near, or exceeding M_{ch} . Finally, a dynamical merger between a CO WD and the CO core of an AGB star in the CD scenario may also produce a SN Ia near M_{ch} (Hoeflich & Khokhlov 1996; Kashi & Soker 2011; Ilkov & Soker 2013; Aznar-Siguán et al. 2015; Noebauer et al. 2016; Maeda et al. 2023).

Comparing the plethora of SNe Ia models is difficult,

as many models can reproduce the broad homogeneity of SNe Ia at peak light. However, at phases before peak light, especially those shortly after the explosion, model predictions diverge significantly because of differences in the initial conditions of a model most strongly reflected in the outermost layers of the ejecta. The outermost layers of the expanding ejecta are the first to become optically thin. Thus, observing these outermost layers of the ejecta requires early observations shortly after the explosion. For example, the origin of high-velocity ($\sim 20000 \text{ km s}^{-1}$, Benetti et al. 2004, 2005; Wang et al. 2009; Harvey et al. 2025) Si and Ca features in early-time optical spectra is still not well understood, with potential explanations including ionization effects (e.g., Blondin et al. 2013), an increased amount of ejecta at high velocities from the explosion (e.g., Mazzali et al. 2005; Tanaka et al. 2006; Kato et al. 2018), material swept up by the ejecta after the explosion (e.g., Gerardy et al. 2004), or interaction with circumstellar material (e.g., Mulligan et al. 2019).

In addition to potentially depending on the progenitor scenario, high-velocity features may also arise from differences in the explosion mechanism. For example, a later transition from deflagration (subsonic flame propagation) to detonation in the delayed-detonation mechanism increases the ejecta velocities (Iwamoto et al. 1999). Additionally, He detonation models may also produce high-velocity ejecta, depending on the viewing angle (Polin et al. 2019; Boos et al. 2021; Collins et al. 2023, 2024; Boos et al. 2024a). Distinguishing these two models is difficult, but early-time data, in particular NIR spectra, have strong discriminatory power (Hsiao et al. 2019).

In the NIR, spectroscopic features have shallower optical depths than in the optical (Wheeler et al. 1998; Höflich et al. 2002) and thus probe material deeper in the ejecta than the optical regime at the same epoch. While optical features such as Ca II H&K and NIR triplet and Si II $\lambda 6355$ easily saturate (e.g., Hachinger et al. 2008)), NIR features do not, making them important diagnostics of SN Ia physics (see, e.g., Hsiao et al. 2019; Hoogendam et al. 2025; Müller-Bravo et al. 2025, and references therein). One example is tracing the distribution of unburnt carbon in the explosion, which differs between the deflagration (more unburnt carbon) and detonation (less unburnt carbon) models (e.g., Höflich et al. 2002; Kasen et al. 2009). Carbon is more easily measured with the less blended NIR C I features than optical C II features, which suffer severe blending with Si II (e.g., Hsiao et al. 2013, 2015; Marion et al. 2015; Wyatt et al. 2021). Additionally, there are two He features in the NIR (He I 1.083 and 2.058 μm) that can be used to test predictions of He absorption made by some He-detonation models (e.g., Collins et al. 2023; Callan et al. 2024; Collins et al. 2024, although other models do not predict He features, e.g., Boos et al. 2021, 2024a). Unfortunately, few SNe Ia have optical and NIR spectral time series data within two days of the explosion (e.g., Hsiao et al. 2013, 2015; Pearson et al. 2024).

In this manuscript, we present a detailed analysis of SN 2024epr, a nearby SN Ia in the galaxy NGC 1198. Both optical and NIR spectra were obtained within two days of the estimated time of first light, ~ 17 days before maximum light. The Ca II NIR triplet of SN 2024epr is particularly notable because it is extremely high velocity at early times and remains strong throughout the pho-

tospheric phases. We obtained further optical and NIR spectroscopic epochs, with dense spectroscopic sampling in the earliest phases after discovery. Our photometric follow-up observations have a cadence of approximately one to two days during the rise. §2 presents our data set and the data reduction methods. We present the photometric data and analysis in §3 and the spectroscopic data and analysis in §4. We discuss the implications for the explosion mechanism for SN 2024epr in §5. Lastly, we offer a summary and concluding remarks in §6. Throughout this work, we use $H_0 = 72 \text{ km s}^{-1} \text{ Mpc}^{-1}$, $\Omega_m = 0.30$, and $\Omega_{vac} = 0.70$.

2. DATA

The Zwicky Transient Facility (ZTF; [Bellm et al. 2019](#)) discovered SN 2024epr at $(\alpha, \delta) = (03^{\text{h}}06^{\text{m}}11\text{s}.224, +41^{\circ}51'00''.18)$ on UT 2024-03-19 at 05:10:26 (MJD = 60388.2) with a *g*-band magnitude of 19.4 mag ([Sollerman 2024a](#)) and classified it as a pre-peak SN Ia ([Sollerman 2024b](#))¹. The ZTF last non-detection was on UT 2024-03-10 at 03:26:47 (MJD = 60379.1) with a limiting *g*-band magnitude of 18.9 mag. Figure 1 shows the location of SN 2024epr in NGC 1198 within the Pan-STARRS ([Chambers et al. 2016](#)) *r*-band template image and a near-peak image taken by the Young Supernova Experiment (YSE; [Jones et al. 2021](#)) as part of our photometric follow-up (see §2.2).

2.1. Host Galaxy

SN 2024epr exploded in NGC 1198, an elliptical (S0 ^a , [de Vaucouleurs et al. 1991](#)) galaxy with a redshift $z = 0.0053$ ([Huchra et al. 1999](#)). The Milky Way line-of-sight extinction toward NGC 1198 is $E(B - V) = 0.113$ mag ([Schlafly & Finkbeiner 2011](#)). To derive an approximate distance to NGC 1198, we use our assumed cosmological parameters, correct the redshift from the heliocentric to the cosmic microwave background frame, and apply a peculiar velocity correction using a density field derived from the 2M++ redshift catalog ([Lavaux & Hudson 2011](#)). Our derived distance is 22.7 ± 3.5 Mpc ($\mu = 31.76 \pm 0.34$ mag), including a velocity error of 250 km s $^{-1}$ in the error budget. We adopt this distance.

We use the `Blast` ([Jones et al. 2024](#)) tool² to acquire archival host-galaxy photometry and estimate the properties of NGC 1198. `Blast` measures galaxy photometry from the Two Micron All Sky Survey (2MASS; [Skrutskie et al. 2006](#)), the Wide-field Infrared Survey Explorer ([Wright et al. 2010](#)), the Sloan Digital Sky Survey ([Fukugita et al. 1996; York et al. 2000](#)), and the Panoramic Survey Telescope and Rapid Response System (Pan-STARRS; [Chambers et al. 2016](#)) using PSF-matched elliptical apertures and runs `Prospector` SED fits on the data ([Leja et al. 2019; Johnson et al. 2021](#)) with speed engagements from a simulation-based inference (SBI++) from [Wang et al. \(2023\)](#). `Blast` uses the `Prospector- α` model with a non-parametric star-

¹ Note that [Karambelkar et al. \(2024\)](#) report an earlier spectrum within a day of discovery, but this spectrum was not uploaded as part of an official TNS classification report and remains proprietary.

² <https://blast.scimma.org/>.

formation history and parameters/priors (for more information, see Appendix A in [Jones et al. 2024](#)).

For NGC 1198, we find the following host-galaxy parameters: a mass of $\log_{10} M/M_{\odot} = 9.9_{-0.1}^{+0.1}$, a star-formation rate of $\log_{10} \text{SFR/yr} = -2.2_{-1.5}^{+0.6}$, a specific star-formation rate of $\log_{10} \text{sSFR/yr} = -12.1_{-1.3}^{+0.6}$, and a mass-weighted mean stellar age of $8.4_{-1.3}^{+3.5}$ Gyr, confirming visual inspection that NGC 1198 is a quiescent, low-mass, and reasonably compact elliptical galaxy.

We find an angular separation of 22.4'' from the host galaxy, corresponding to a projected separation of ~ 2.5 kpc at the distance of NGC 1198 (22.7 Mpc).

2.2. Photometric Data

Our optical photometry of SN 2024epr is from the Asteroid Terrestrial-impact Last Alert System (ATLAS; [Tonry et al. 2018](#)), YSE, and ZTF surveys, and additional follow-up observations were taken using the Nickel telescope and the Lulin 1m Telescope. Table 1 presents a log of our photometric observations.

ATLAS observes the entire sky multiple times per night with four telescopes in Chile, South Africa, and Hawai'i ([Tonry et al. 2018](#)). It uses “cyan” and “orange” broadband filters that are approximately equivalent to *g+r* and *r+i* bandpasses, respectively. Most observations of SN 2024epr were taken with the orange (*o*) filter, which has a wavelength coverage of 560-820 nm ([Tonry et al. 2018](#)). Data were retrieved from the ATLAS Transient Science Server ([Smith et al. 2020; Shingles et al. 2021](#)), and same-night data were stacked using a weighted average, excluding data affected by clouds.

YSE is a time-domain survey on the Pan-STARRS telescopes surveying ~ 1500 deg 2 of sky at a time with a three-day cadence in the *griz* filters. For particular targets of interest, including SN 2024epr, observations at 1- or 2-day cadence are obtained in *grizy*. The Pan-STARRS observations were reduced using the `Photpipe` package ([Rest et al. 2005](#)) as implemented by the YSE team ([Jones et al. 2021; Aleo et al. 2023](#)). We used the YSE-PZ target and observation manager ([Coulter et al. 2022, 2023](#)) to compile the data for this SN.

ZTF is a time-domain survey currently providing public, two-day cadence *g*- and *r*-band data for the northern extragalactic sky. We obtained ZTF photometry using the ZTF forced photometry service ([Masci et al. 2019](#))³.

Follow-up observations from the Nickel and Lulin telescopes used CCD imagers. Point-spread-function photometry is measured from the images and calibrated by comparing field stars to the Pan-STARRS photometric catalog ([Flewelling et al. 2020](#)), using standard bias and sky-flat-field procedures.

After uploading to arXiv, two of us (R.P. and P.C.) contacted the other authors with additional images taken with the Corrected Dall-Kirkham 24'' and Ritchey-Chretien 32'' telescopes by R.P. at the Post Observatory. The images were taken with Sloan filters produced by Astrodon with Pan-STARRS archival images as the template for image subtraction. The photometric calibration is against the SDSS magnitudes transformed from the Pan-STARRS photometric catalog ([Flewelling et al. 2020](#)).

³ <https://irsa.ipac.caltech.edu/Missions/ztf.html>.

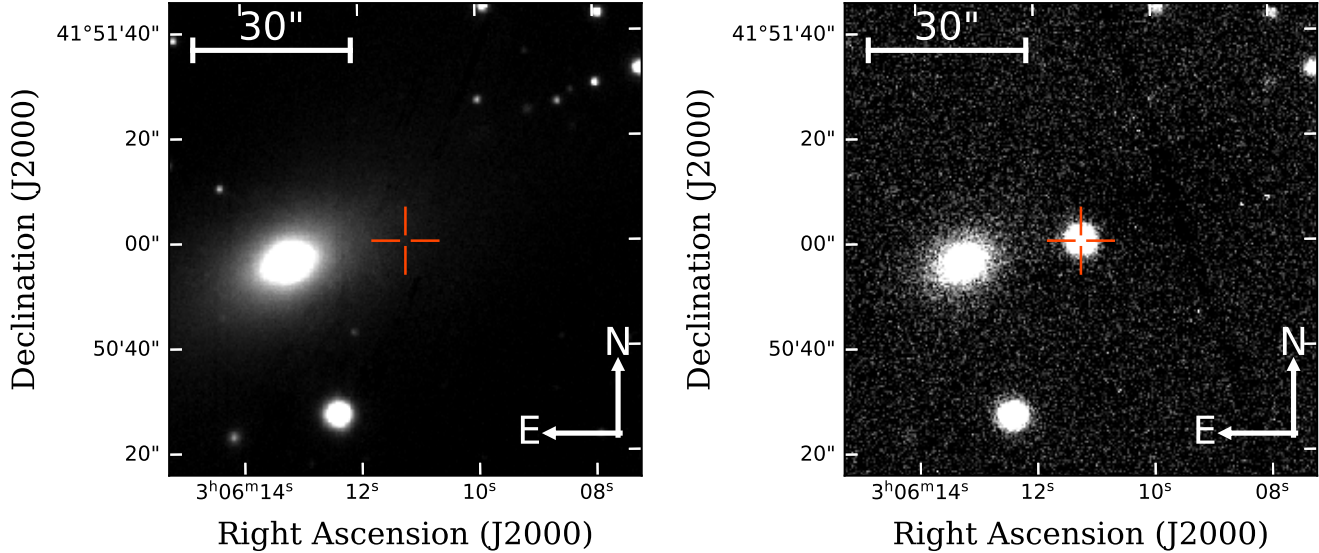


FIG. 1.— Finder charts for SN 2024epr. *Left*: Archival Pan-STARRS r -band image before explosion (Chambers et al. 2016; Flewelling et al. 2020; Magnier et al. 2020). *Right*: Pan-STARRS r -band image on UT 2024-04-08 at 05:45:08 (MJD = 60408.2) by YSE.

TABLE 1
Log of the photometric observations of SN 2024epr. The full table is available on the arXiv listing.

MJD	Filter	m	σ_m	Source
60374.19	g	22.64	99.99	ZTF
60375.30	o	18.46	99.99	ATLAS
⋮	⋮	⋮	⋮	⋮
60652.12	g	19.52	0.18	ZTF

NIR YJH photometry was obtained with the Wide Field Camera (WFCAM; Casali et al. 2007; Hodgkin et al. 2009) mounted on the University of Hawai’i-owned and operated UKIRT 3.8m telescope. We again processed these data with Photpipe and calibrated them using 2MASS following Hodgkin et al. (2009) and Peterson et al. (2023). We used unforced, non-difference-imaged photometry from DOPHOT (Schechter et al. 1993). Because SN 2024epr was bright and located near the outskirts of a smooth elliptical galaxy, a local background estimation and centroid determinations from individual images were considered sufficient for reliable photometry.

2.3. Spectroscopic Data

We obtained 16 optical and 10 NIR spectra of SN 2024epr. The first public spectrum (from Sollerman 2024a) was taken by the Nordic Optical Telescope (NOT) using the Alhambra Faint Object Spectrograph and Camera (ALFOSC)⁴. Seven further optical spectra were taken on the UH2.2m telescope using the Super-Nova Integral Field Spectrograph (SNIFS; Lantz et al. 2004) as part of the Spectroscopic Classification of Astrophysical Transients (SCAT; Tucker et al. 2022) survey, with reductions using the standard SCAT pipeline (Tucker et al. 2022). One spectrum was taken with the Keck Cosmic Web Imager (KCWI; Morrissey et al. 2018;

TABLE 2
Log of the optical spectroscopic observations of SN 2024epr. The reported rest-frame phases are with respect to the time of B -band maximum on MJD 60406.6.

UT Date	MJD	Phase [days]	Telescope	Spectrograph	R
2024-03-20	60389.8	-16.6	NOT	ALFOSC	710
2024-03-23	60391.2	-15.3	UH88	SNIFS	2000
2024-03-24	60392.2	-14.2	UH88	SNIFS	2000
2024-03-27	60396.2	-10.3	Lick	KAST	1800
2024-04-06	60406.2	-0.3	UH88	SNIFS	2000
2024-06-27	60488.6	+81.6	UH88	SNIFS	2000
2024-07-05	60496.6	+89.6	UH88	SNIFS	2000
2024-07-07	60498.5	+91.4	Lick	KAST	1800
2024-07-19	60510.6	+103.5	UH88	SNIFS	2000
2024-08-06	60528.4	+121.2	Lick	KAST	1800
2024-08-09	60531.6	+124.4	UH88	SNIFS	2000
2024-08-27	60549.5	+142.1	Lick	KAST	1800
2024-09-05	60558.6	+151.3	Keck II	KCWI	900
2024-09-13	60566.5	+159.0	Lick	KAST	1800
2024-09-24	60577.4	+169.9	Lick	KAST	1800
2024-10-03	60586.5	+179.0	Lick	KAST	1800

McGurk et al. 2024). We extracted the 1D spectrum using a custom pipeline from the automatic KCWI data reduction pipeline-produced data cubes⁵. Seven optical spectra were observed by the Shane 3m Telescope using the Kast Double Spectrograph (Miller & Stone 1994). The Kast data were reduced using the UCSC Spectral Pipeline⁶ (Siebert et al. 2020). Table 2 compiles the optical spectroscopic observations.

Seven NIR spectra were taken on the Gemini North 8m telescope using the Gemini Near-Infrared Spectrograph (GNIRS; Elias et al. 2006b,a). Reductions were performed using standard PYPEIT procedures (Prochaska et al. 2020a). An additional spectrum was taken using NASA’s InfraRed Telescope Facility (IRTF) with SpeX (Rayner et al. 2003). Finally, the Keck Infrared

⁵ The documentation for which is available online.

⁶ See the online documentation.

⁴ Accessed via <https://www.wis-tns.org/object/2024epr>.

TABLE 3
Log of the NIR Spectroscopic Observations of SN 2024epr. The reported rest-frame phases are relative to the B -band maximum time on MJD 60406.6.

UT Date	MJD	Phase [days]	Telescope	Spectrograph	R
2024-03-21	60390.1	-16.5	Gemini	GNIRS	1500
2024-03-22	60391.2	-15.3	IRTF	SpeX	80
2024-03-23	60392.0	-14.5	Gemini	GNIRS	1500
2024-03-30	60398.8	-7.8	Gemini	GNIRS	1500
2024-04-06	60406.2	-0.4	Gemini	GNIRS	1500
2024-07-05	60496.6	+89.6	Keck II	NIRES	2700
2024-07-06	60497.5	+90.4	Gemini	GNIRS	1500
2024-07-27	60518.5	+111.4	Gemini	GNIRS	1500
2024-09-04	60557.5	+150.2	Gemini	GNIRS	1500
2024-09-12	60565.5	+158.1	Keck II	NIRES	2700

Transients Survey (Tinianont et al. 2024) obtained two post-peak transitional-phase NIR spectra with the Near-InfraRed Echellette Spectrometer on Keck II (NIRES; Wilson et al. 2004). The GNIRS, NIRES, and SpeX data were reduced with telluric corrections from an A0V star using the standard PypeIt (GNIRS and NIRES; Prochaska et al. 2020b) or Sextool (SpeX; (Cushing et al. 2004)) procedures. Table 3 catalogs our NIR spectroscopic observations.

3. PHOTOMETRY

3.1. Light Curves

Figure 2 shows the optical and NIR photometry for SN 2024epr, along with SuperNovae in object-oriented Python (SNooPy; Burns et al. 2011, 2014) fits (using the `max_model`, see following discussion) to the Post Observatory and Pan-STARRS data. While we do not have B -band data near maximum light, SNooPy computes SED fits whose synthetic photometry is used to return parameters with respect to the B band. Using `EBV_model12` with $\Delta m_{15}(B) = 1.09$ mag as a prior (from the `max_model` fit described below), the SNooPy fit finds a host-galaxy extinction of $E(B-V) = 0.12 \pm 0.07$ mag and peak B -band magnitude of 13.80 ± 0.01 mag.

The SNooPy `EBV_model12` model fits the light curve of SN 2024epr reasonably well in the gzy bands, with worse fits in the ri bands. The issues in the ri bands may be due to the significant Si and Ca absorption, respectively, which could cause band-dependent shifts in color relative to a typical reddening law (see Section 4.1). We consider the high extinction measurement to be most likely due to the unusual colors of 2024epr or the fact that SNooPy may not fully model variation in SN intrinsic colors (Burns et al. 2014).

Since SN 2024epr has peculiar color evolution (see §3.2), we report the `max_model` values for t_{peak}^B , which is on MJD 60406.6 ± 0.4 , $\Delta m_{15}(B) = 1.09 \pm 0.07$ mag, and $s_{BV} = 1.189 \pm 0.04$. The gri peak magnitudes are 13.23 ± 0.04 mag, 13.07 ± 0.04 mag, and 13.76 ± 0.03 mag, respectively.

Finally, the ATLAS last non-detection is notably deep. The 3σ upper limit is 19.40 mag and the 5σ upper limit is 18.85 mag. Correcting for the Milky Way extinction ($A_o = 0.27$ mag) and host-galaxy distance, this yields 3σ and 5σ absolute magnitude limits of -12.64 mag and -12.08 mag, respectively.

We emphasize that we do not directly measure $\Delta m_{15}(B)$ or s_{BV} because our data do not extend to the necessary time scales to do so (15 days and 20-40 days, respectively; Burns et al. 2014). Rather, we infer it from fitting the rising light curve with SNooPy. To ensure the accuracy of our computed $\Delta m_{15}(B)$ (and of the time of maximum light), we compare our phase-shifted light curves with SN 2020jgl (Galbany et al. 2025), another SN Ia with strong and high-velocity Ca II absorption at early times (see §4 for spectral comparison). Figure 3 shows the overlaid light curves of SNe 2020jgl and 2024epr shifted to the rest-frame phase with respect to the epoch of peak B -band magnitude and shifted by the difference in distance modulus between the two host galaxies. The light curves agree well using the SNooPy `max_model` peak times for SN 2024epr. SN 2020jgl has a similar $\Delta m_{15}(B)$ value ($\Delta m_{15}(B) = 1.111 \pm 0.018$ mag, Galbany et al. 2025) to our inferred $\Delta m_{15}(B)$ value for SN 2024epr.

We also fit the data with the SALT3 model (Kenworthy et al. 2021; Taylor et al. 2023) and see similar color discrepancies in both the early-time and near-maximum data, with the i -band flux in particular lower than the best-fit model. Again, we interpret this as an indication of stronger-than-normal Ca absorption affecting this band. The best-fit SALT parameters for SN 2024epr are a relatively red $c = 0.19 \pm 0.02$ mag, a slightly fast (but uncertain) decline rate of $x_1 = -0.39 \pm 0.33$, and a somewhat underluminous B -band absolute magnitude that is approximately 0.7 mag fainter than the mean SN Ia at that redshift; however, adopting a peculiar velocity uncertainty of 250 km/s at the redshift of SN 2024epr gives an additional magnitude uncertainty ~ 0.34 mag. Using the SALT nuisance parameters from Brout et al. (2022) gives a distance modulus to NGC 1198 of 31.90 ± 0.11 mag, closer than the SNooPy distance. For the rest of this work, we adopt the host-galaxy redshift distance from §2.1.

Our inferred $\Delta m_{15}(B)$ value is somewhat inconsistent with SN 2024epr being a Branch et al. (2006) “cool” object (see 4.1) and the similarities in the NIR spectra to subluminous SNe Ia (see 5.3.3). In light of this, we also estimate $\Delta m_{15}(B)$ based on the relationship between $\mathcal{R}(\text{Si})$ (the ratio of the Si II $\lambda 5972$ and $\lambda 6355$ pEWs at peak light; see Nugent et al. 1995) and $\Delta m_{15}(B)$ presented in Benetti et al. (2005), which gives $\Delta m_{15}(B) \approx 1.3$ mag⁷.

Correcting for the distance and the Milky Way extinction, we find that the B -band absolute magnitude of SN 2024epr is $M_B \approx -18.4 \pm 0.4$ mag. We correct for SN color by adopting the `EBV_model12` host-galaxy extinction and $R_B = R_V + 1 = 3.2$, since the median R_V for SNe Ia is known to be lower than that of the Milky Way (e.g., Burns et al. 2014). This is likely not from actual host-galaxy extinction but rather reflects the known empirical correlation between SN color and luminosity (e.g., Burns et al. 2014). After this correction, SN 2024epr is consistent within uncertainties with normal SNe Ia (Figure 4). Its slightly subluminous location could be explained by a variety of factors, including a poor distance estimate to the host and the lack of a B -band peak measured directly from the data, rather than inferred from an SED that

⁷ Benetti et al. (2005) do not fit the data, so we estimate by eye.

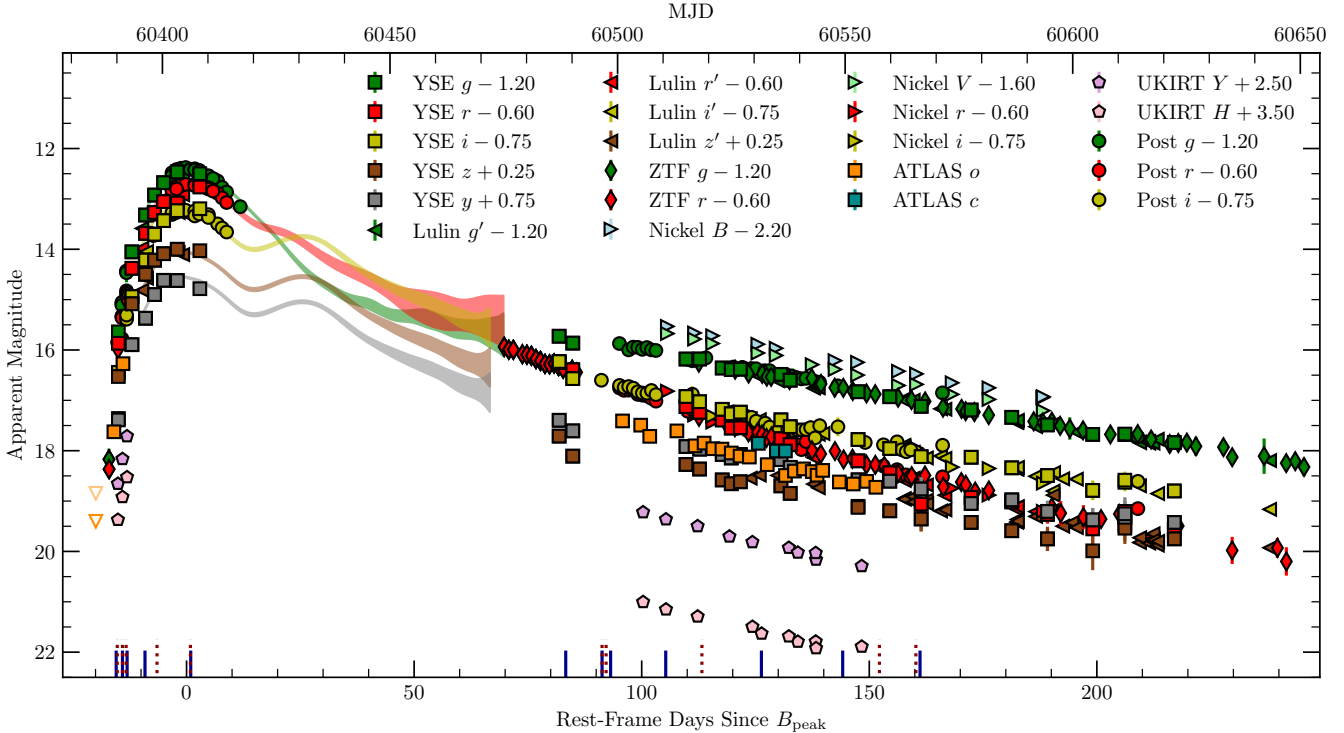


FIG. 2.— The optical and NIR photometry of SN 2024epr. Unfilled triangles represent photometric upper limits. The shaded regions denote model fits described in §3.1. Spectroscopic observations are shown as solid blue (optical) and dotted red (NIR) lines on the bottom of the figure. The ATLAS non-detection is 5σ .

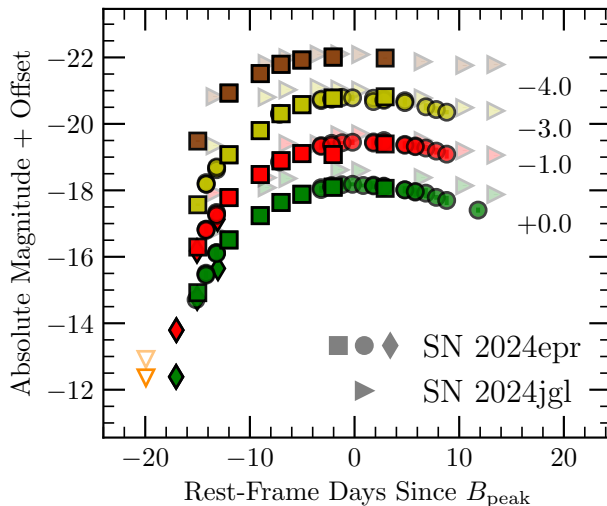


FIG. 3.— Comparison of the rising YSE light curves of SN 2020jgl (right-facing triangles; from YSE DR1 Aleo et al. 2023) and SN 2024epr. Circles, squares, and diamonds denote Post, YSE, and ZTF photometry, respectively. The ATLAS 3σ (bold) and 5σ (light) last nondetections are orange, downward triangles; there are no ZTF non-detections a week before discovery. Photometric bands are, from the bottom up, *griz*. When shifted by peak time, the light curves line up, confirming that the SNooPy time of *B*-band maximum is reliable. Offsets (not including the 0.67 mag difference in the host-galaxy distance moduli) are reported next to each band.

may only superficially match that of SN 2024epr. The peculiar-velocity-induced distance uncertainty is also a non-negligible factor in the absolute magnitude uncertainty. We estimate this uncertainty assuming a peculiar

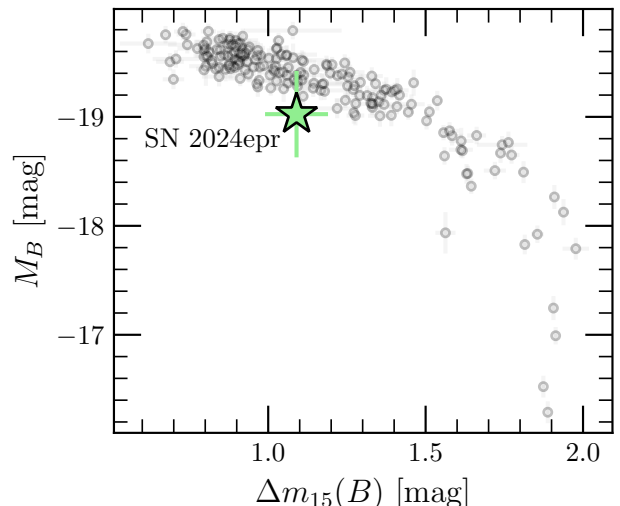


FIG. 4.— SN 2024epr (light green star) on the luminosity-width relationship (Phillips 1993). SN 2024epr is a normal SN Ia when corrected for Milky Way extinction and SN color as described in the text. We infer the distance from the host-galaxy redshift (there is no independent distance to NGC 1198), assuming a peculiar velocity error of 250 km s^{-1} . The uncertainty in distance is the dominant source of luminosity uncertainty. The *B*-band magnitude is computed using SED fit from SNooPy.

velocity of 250 km s^{-1} (Peterson et al. 2022).

3.2. Color Curves

Figure 5 shows the Milky Way extinction-corrected $g - r$, $r - i$, and $i - z$ color curves for SN 2024epr compared to the Milky Way extinction-corrected colors for

SN 2020jgl, another SN Ia with strong Ca II features, and well-observed normal SNe Ia from the YSE DR1 sample (SNe 2020nlb, 2020opy, 2020uxz, 2021J, 2021hiz, 2021hpr, 2021pfs; Aleo et al. 2023).

SNe 2020jgl and 2024epr are similar to the comparison SNe Ia in the $g - r$ color throughout their evolution. Interestingly, despite the similarity in the $g - r$ and $i - z$ colors, SNe 2020jgl and 2024epr differ from the other SNe Ia in their $r - i$ color curve, being much flatter ($r - i \approx 0$ mag from pre-peak to maximum light) and not showing any color evolution until 10 days past B -band maximum. This implies the color difference is not solely due to reddening. One possible explanation is that, at early times, the high-velocity Ca feature is so blue-shifted that the Ca absorption trough is solely in the i band (see §4.1). This difference may explain why the early-time $i - z$ color is much redder than that of the comparison SNe Ia, similar to what is seen for SN 2021aefx, which exhibits a high-velocity Ca II H&K feature (Ashall et al. 2022).

Another SN Ia with similarly low luminosity for its measured $\Delta m_{15}(B)$ is SN 2006bt (Foley et al. 2010), which also has peculiar colors; however, the colors shown by SN 2020jgl and 2024epr ($r - i \approx +0.3$ mag) at maximum light are much redder than SN 2006bt ($r - i = -0.3$ mag), suggesting that SN 2024epr is unlike SN 2006bt, which also had significantly slower velocities.

4. SPECTROSCOPY

4.1. Optical Spectra

Figure 6 presents the optical spectroscopic time series of SN 2024epr. The spectra include some of the earliest optical spectra of a SN Ia, with rest-frame phases ranging from -16.6 to $+159.0$ days relative to the B -band peak. The optical spectra look like a typical SN Ia but with high velocities at early times and a much stronger Ca II NIR triplet.

4.1.1. Early-Time Comparison

We compare our photospheric spectra to the earliest (-15.3 days) and peak-light (-0.3 days) SNIFS spectra of SN 2011fe (Pereira et al. 2013) in Figure 7. The most notable difference is the strength and high-velocity ($\sim 35\,000$ km s $^{-1}$ versus $\sim 20\,000$ km s $^{-1}$) of Ca II in SN 2024epr versus SN 2011fe at ~ -16 days. On the other hand, the Si II feature has a similar velocity to SN 2011fe, albeit slightly faster, and the C II $\lambda 6580$ feature is at the same velocity as SN 2011fe.

In Figure 8, we broaden our comparison sample to include the following SNe Ia: SN 2009ig (Foley et al. 2012), SN 2011fe (Pereira et al. 2013), SN 2012fr (Chidress et al. 2013), SN 2017cbv (Hosseinzadeh et al. 2017), SN 2020jgl (Galbany et al. 2025), and SN 2021aefx (Ashall et al. 2022; Hosseinzadeh et al. 2022). These SNe were all classified as normal SNe Ia and were chosen due to the availability of their early-time optical spectra, and some, such as SNe 2020jgl and 2021aefx, are known to have high-velocity Ca II features (Ashall et al. 2022; Galbany et al. 2025).

In their earliest spectra, SNe 2020jgl and 2024epr have stronger and faster Ca II NIR than the comparison SNe Ia, with the extremely high velocity causing the feature to blend with the O I $\lambda 7774$ feature. The other

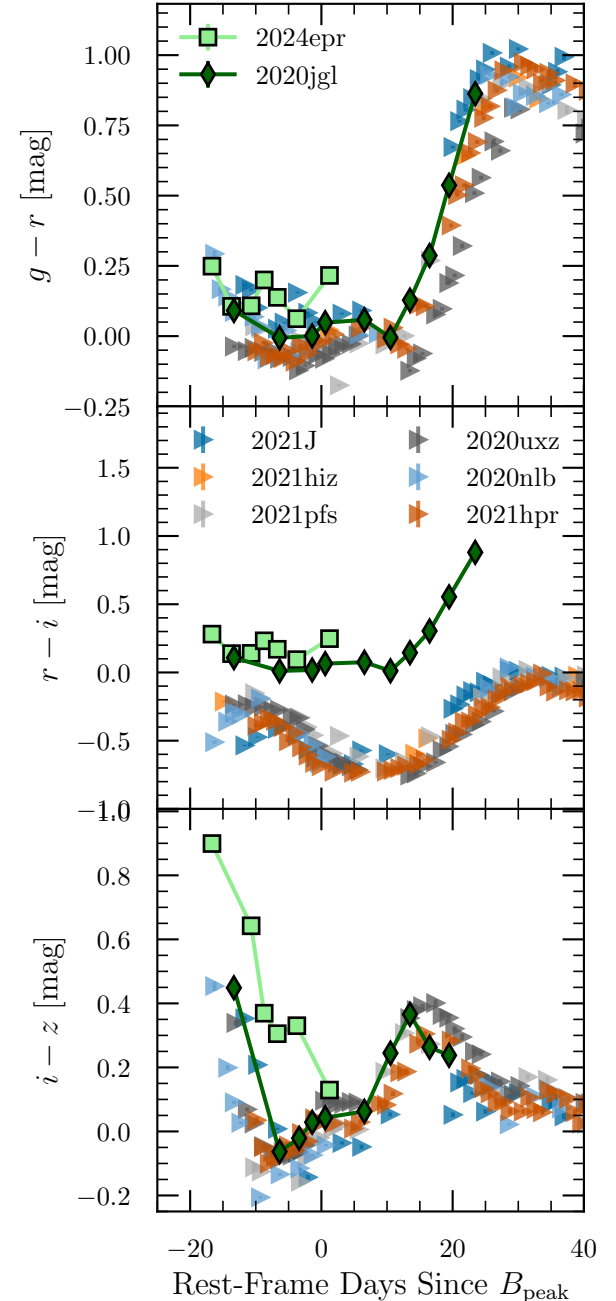


FIG. 5.— Milky-Way extinction-corrected color curves of SNe Ia with strong Ca II NIR features (SNe 2020jgl and 2024epr) compared to normal SNe Ia from YSE DR1 (Aleo et al. 2023). The two SNe Ia with strong Ca II, SNe 2020jgl and 2024epr, are redder than the normal SNe Ia.

events with high-velocity Ca features (2009ig, 2012fr and 2021aefx) do not show strong O I $\lambda 7774$, with a weak, $\sim 20\,000$ km s $^{-1}$ O I feature in SN 2021aefx and no clear O I in SNe 2009ig or 2012fr. At slightly later epochs, 14 and 13 days before maximum light, the spectra are largely similar to the -15 day spectra, and even at -9 days the O I and Ca II features are still slightly blended.

Like the O I and Ca II features, the Si II $\lambda\lambda 5972, 6355$ features blend in SNe 2020jgl and 2024epr, with some Si II $\lambda 6355$ at $\sim 35\,000$ km s $^{-1}$ in the earliest spectrum.

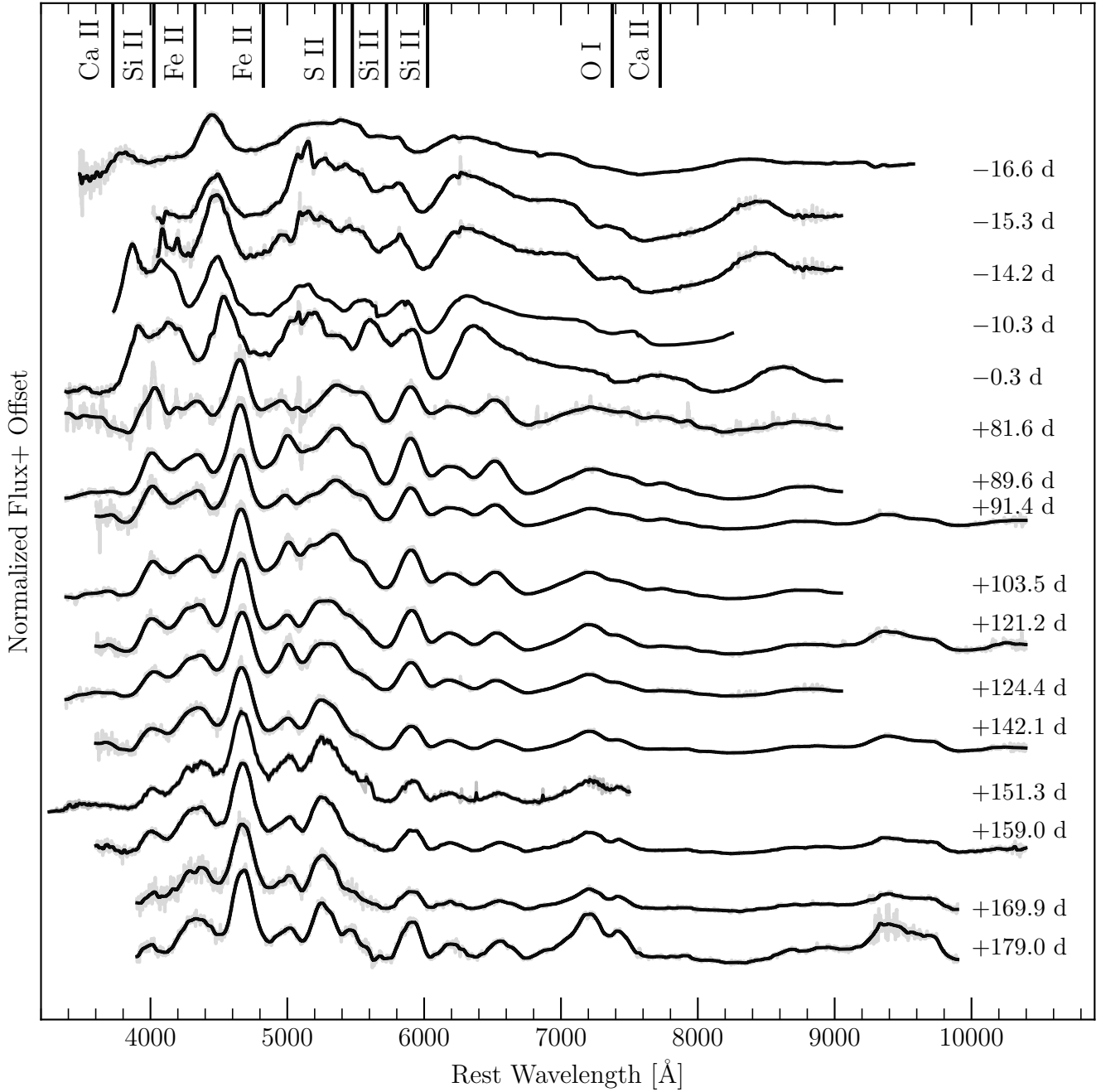


FIG. 6.— Time series of optical spectra for SN 2024epr (grey unsmoothed; black smoothed). Epochs are with respect to B -band maximum on MJD 60406.6. Spectrographs are listed in Table 2.

Unlike O I and Ca II features, the Si features become less blended a day later, and by -13 days the two features have only minimal blending. At 9 days before maximum light, the Si II features are no longer blended, and SN 2024epr has the strongest Si II $\lambda 5972$ out of all the plotted SNe Ia.

On the red edge of the Si II $\lambda 6355$, each SN Ia shows a potential flattening or notch feature in their earliest spectrum, which Thomas et al. (2011b) attribute to C II $\lambda 6580$. The strongest feature is seen in SN 2017cbv at early times, with the C II feature equaling the Si II $\lambda 6355$ feature in depth. A clear notch is seen in SN 2011fe, with

tentative C II features seen in SNe 2020jgl and 2021aefx. SN 2024epr may have a notch similar to SN 2011fe; however, the feature's location also corresponds to an O₂ skyline. Given the other O₂ skyline at 6800 in our -16.6 day spectrum and evidence of sky subtraction issues in the subsequent two, we cannot confidently claim a C II $\lambda 6580$ feature in SN 2024epr.

As discussed in §4.2, we also find evidence for the presence of C in SN 2024epr at early times by identifying a C I feature in the NIR spectra at the same epoch (see Figs. 15 and 17), highlighting the power of contemporary optical and NIR spectroscopic coverage. Except for

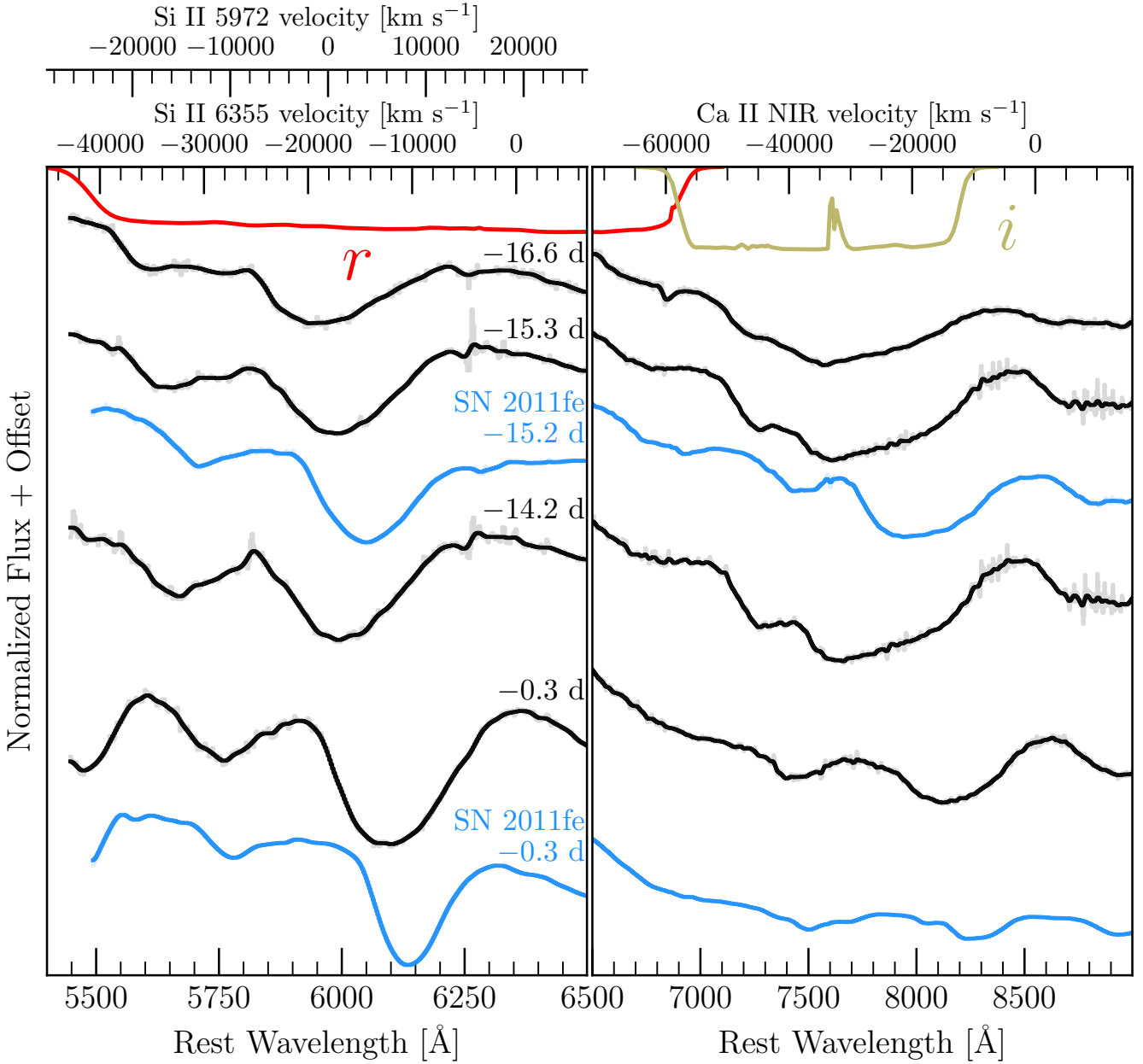


FIG. 7.— Comparison of the early-time spectral time series data of SN 2024epr (unsmoothed grey, smoothed black) with that of SN 2011fe (blue). *Left:* the spectral region around Si II $\lambda 6355$. *Right:* spectral region around the Ca NIR triplet. Epochs are with respect to *B*-band maximum on MJD 60406.6, and the *i*-band transmission function is shown in dark khaki on the top of the left panel.

SNe 2011fe and 2017cbv, the C II feature disappears from the SNe Ia spectra within a few days after the first spectrum implying that the C may be located in the outermost layers.

Finally, the morphology of the Fe II, Si II and Fe III blend between 4600 Å and 5000 Å shows SNe 2020jgl and 2024epr are very similar to each other and have approximately the same features at the same velocities as SNe 2009ig, 2011fe, and 2021aefx. This explains the early-time color curves of SNe 2020jgl and 2024epr when compared to the normal YSE sample: colors using bluer bands (e.g., $g - r$) match the colors of normal SNe Ia better than colors using redder filters (e.g., $i - z$), as discussed in §3.2.

4.1.2. Peak-Light Comparison

Figure 9 shows the spectra at the time of maximum light. Here, SNe Ia with faster early-time velocities (e.g., SNe 2009ig, 2020jgl, 2021aefx, and 2024epr) generally have faster peak-time velocities. Still, peak velocities are within the standard range of SNe Ia velocities. Of the high-velocity SNe Ia, SN 2024epr has the strongest secondary Si II feature; SNe Ia with high-velocity early-time features generally show weaker secondary Si II, in contrast to SN 2024epr.

4.1.3. Pseudo-Equivalent Widths and Velocities

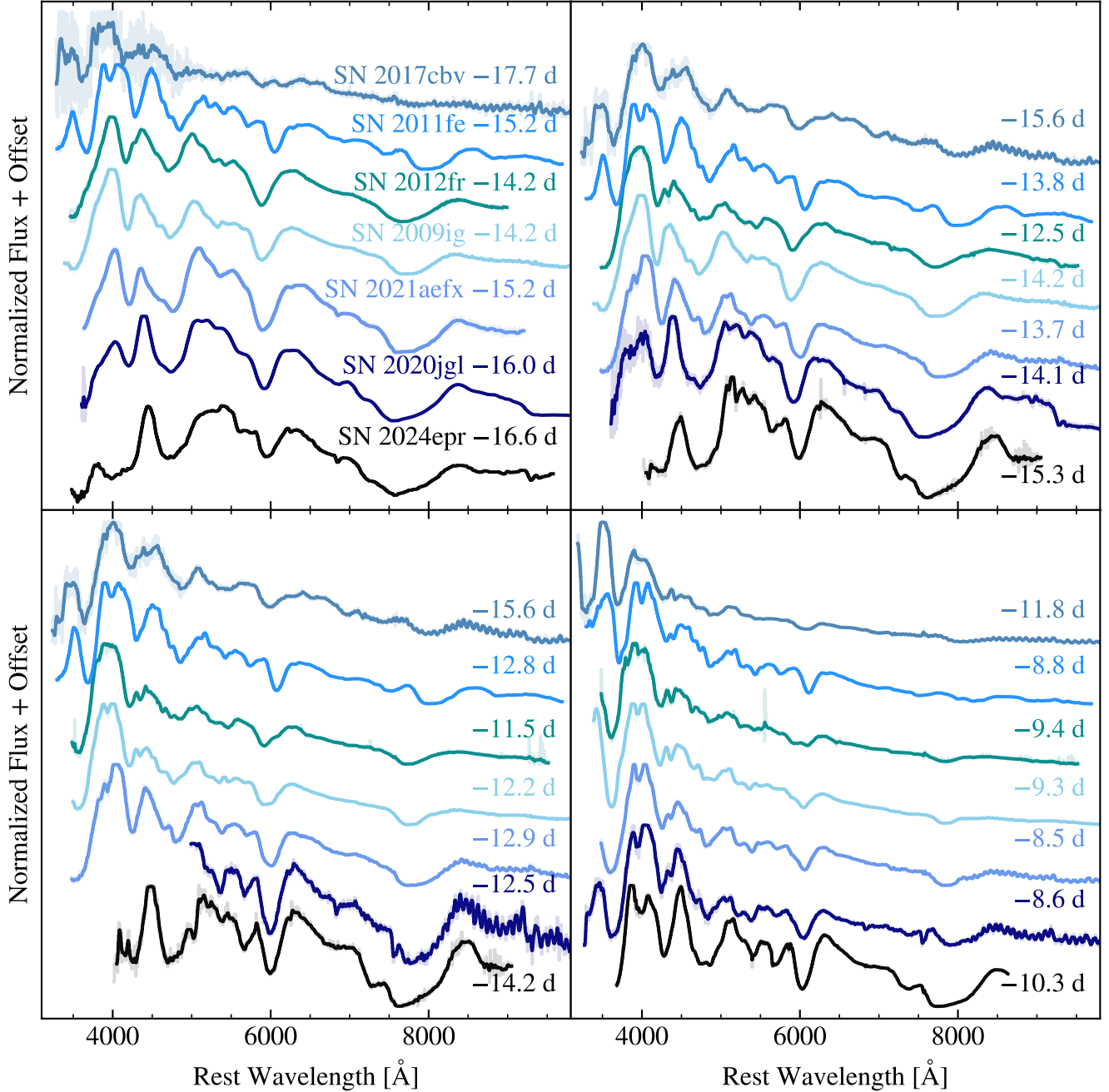


FIG. 8.— Comparison of SN 2024epr (black, bottom) to other SNe Ia with early-time spectroscopic time series data. The plotted order is SN 2017cbv, SN 2011fe, SN 2012fr, SN 2009ig, SN 2021aefx, and SN 2020jgl from top to bottom in each panel.

To quantify spectral differences, we use the Python package `misfits`⁸ to measure the pseudo-equivalent width (pEW) and velocity for each feature in each spectrum (for a description of `misfits` and the routines used, see Hoogendam et al. 2022 and Holmbo et al. 2023). We note that when fitting the high-velocity Ca II triplet, it blends with the O I $\lambda 7774$ feature. Thus, we fit three features in this case: one for the O I $\lambda 7774$ feature and two for the Ca II triplet feature, which has a high-velocity and photospheric-velocity component.

Figure 10 shows the Branch et al. (2006) classification

scheme, which classifies SNe Ia into four groups based on the pEW of the Si II $\lambda\lambda 5972$ and 6355 features. The “core normal” SNe Ia are a highly homogeneous group with similar spectral features. For “broad line” SNe Ia, the Si II $\lambda 6355$ feature is broader than the core normal SNe Ia, perhaps indicating a high-velocity component to the feature. Alternatively, “shallow silicon” SNe Ia have shallower Si II features, especially the weaker Si II $\lambda 5972$ feature, which may be entirely absent from the SN Ia spectrum. As shallow silicon SNe Ia tend to be overluminous, a likely explanation is the explosion energy is high enough to doubly ionize Si, resulting in Si III features in-

⁸ <https://github.com/sholmbo/misfits>

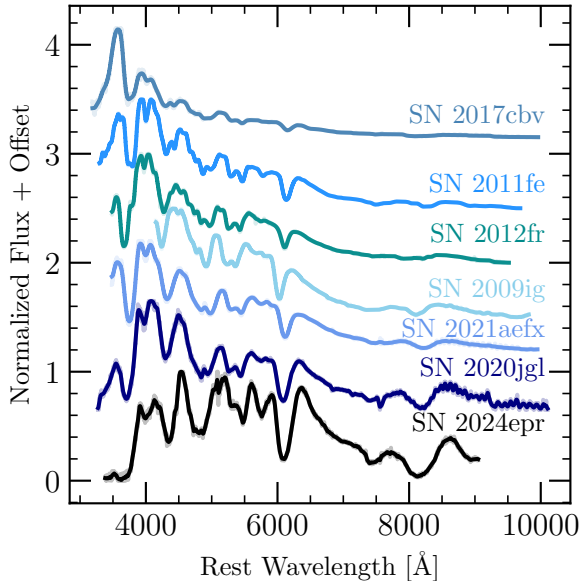


FIG. 9.— Near maximum light comparison of SN 2024epr to the same SNe Ia as Figure 8.

stead of Si II. Finally, the “cool” SNe Ia have a stronger Si II $\lambda 5972$ features due to a lower temperature compared to the core normal SNe Ia. In the canonical Branch et al. (2006) scheme, SN 2024epr is a “cool” SN Ia, with a strong secondary Si II feature at max (pEWs of ~ 43 Å and ~ 149 Å for Si II $\lambda \lambda 5972$ and 6355, respectively). This is dissimilar to SN 2020jgl (pEWs of 7 Å and 142 Å, respectively), which has a weaker Si II $\lambda 5972$ at peak.

We also construct a pseudo-Branch et al. (2006) diagram in the bottom panel of Figure 10 to compare the Ca II pEW (~ 525 Å for SN 2024epr, and ~ 257 Å for SN 2020jgl) to that of Si II $\lambda 6355$. In general, we see that core normal and shallow-silicon SNe Ia tend to have smaller Ca II pEW and are generally distinguishable from the broad line and cool SNe Ia as in the standard Branch et al. (2006) diagram. However, unlike the standard Branch et al. (2006) diagram, the broad line and cool SNe Ia overlap in the Ca II NIR diagram. This is explained by the Ca II NIR triplet saturating more easily than Si II $\lambda 5972$. Additionally, there is a weak linear correlation for all SNe Ia between the Si II $\lambda 6355$ and Ca II NIR pEWs at maximum light. SN 2020jgl is consistent with this trend despite its strong early-time Ca II NIR feature, but SN 2024epr is not. Of the plotted SNe Ia, SN 2024epr has the largest Ca II pEW, indicative of a higher-than-usual abundance of Ca.

4.2. NIR Spectra

Figure 11 presents our pre-peak NIR spectroscopic time series data for SN 2024epr. The spectra show common SN Ia NIR features such as Mg II 1.0092 μm , C I 1.0693 μm , and Mg II 1.0927 μm (Hsiao et al. 2013, 2015; Marion et al. 2015; Hsiao et al. 2019; Lu et al. 2023).

The absorption feature at 1.06 μm in the first spectrum may be high-velocity ($\sim 20\,000$ km s^{-1}) O I 1.1286 , 1.1302 μm , high-velocity ($\sim 40\,000$ km s^{-1}) C I 1.1754 μm , or Fe III 1.1323 μm . There are difficulties with each of these interpretations for the 1.06 μm

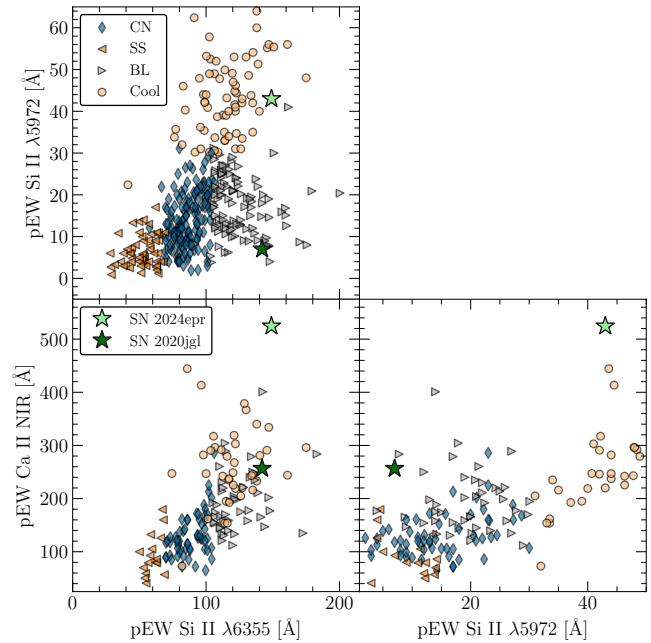


FIG. 10.— Branch diagram (comparison of SN Ia spectral features at maximum light; classifications based on Branch et al. 2006) with SN 2024epr as the light green star and SN 2020jgl as the dark green star. The other SNe Ia data are from Blondin et al. (2012), Folatelli et al. (2013), Hoogendam et al. (2022), and Morell et al. (2024). Top: Canonical Branch et al. (2006) diagram with the two Si II lines as diagnostics. Bottom: Pseudo-Branch diagram with the Ca II NIR feature replacing the Si II $\lambda 5972$ feature. While SN 2024epr is an unremarkable “cool” SN Ia in the canonical Branch scheme, when using the Ca II line as a diagnostic, SN 2024epr is more extreme than any other SN Ia plotted.

feature. First, the optical O I is present in every optical spectrum, whereas this feature is not seen in subsequent spectra of SN 2024epr. Second, if it is C I 1.1754 μm , it would be higher velocity than C I 1.0693 μm . Finally, if the feature is from Fe III recombining into Fe II, the presence of Fe III in the outermost layers of the ejecta within a day after the explosion requires higher temperatures (see, e.g., DerKacy et al. 2020) for a short time after the explosion before cooling from expansion. However, a higher temperature at such early times contradicts the presence of Si II $\lambda 5972$ at early times, a hallmark spectral feature of cooler explosions.

The next redward absorption feature is at 1.124 μm , which Höflich et al. (2002) attribute to Mg II 1.1620 and 1.1600 μm . If so, the velocity of this feature is much slower than the bluer Mg II 1.0927 μm feature. Given the paucity of features in this region (see, e.g., the line list of Marion et al. 2009), Mg II may be the best option despite this velocity inconsistency.

Hsiao et al. (2019) identify the minimum at 1.23 μm as a blend of Si III 1.2523 and 1.2601 μm . Other Si III features include Si III 1.3395 , 1.3497 , and 1.3644 μm , which we do not observe in SN 2024epr at early times, but may appear near peak. Alternatively, the models of Höflich et al. (2002) predict weak O I 1.3164 μm features near 1.23 μm , which we may see given the strong O I $\lambda 7774$ feature in the optical.

Si/Mg/Co blends dominate the H and K -band regions of the spectra (Höflich et al. 2002; Marion et al. 2009). In the H band, the bluest edge is determined

by Mg II 1.6787 μm and the red emission from the P Cygni profile is from Co II 1.5759, 1.6064, 1.6361, 1.7772, 1.7462 μm (Marion et al. 2009; Ashall et al. 2019a,b). The K -band has Mg II 2.1569 μm , Mg II 2.1369, 2.1432, 2.4041, 2.4044, 2.4125 μm , Si II 2.1920 and 2.1990 μm (Höflich et al. 2002), and Co II 2.1350, 2.2205, 2.3613, 2.4596 μm (Marion et al. 2009) features.

After the seasonal break, we obtained additional NIR spectra. Spectra starting \sim 90 days after peak light trace the transition between the end of the photospheric phase with an optically thick, emitting photosphere and the beginning of the nebular phase when the ejecta are optically thin. These spectra are dominated by the permitted Fe II and Co II features (Marion et al. 2009; Gall et al. 2012; Friesen et al. 2014) which fade as the SN Ia evolves and eventually forbidden emission dominates the spectrum \sim 1 year after explosion.

Figure 12 compares the late-time NIR spectra of SN 2024epr with other SNe Ia during the photospheric/nebular transition phase, and it includes several never-before-published spectra of SN 2011fe (PI: Phillips). These spectra were taken by Gemini/GNIRS and accessed through the Gemini Science Archive (Hirst & Cardenes 2017). The three spectra were observed on MJDs 55927.6, 55945.5, and 56038.5. We reduced these spectra in the same manner as the spectra of SN 2024epr (see §2.3).

Additional spectra come from Sand et al. (2016), Lu et al. (2023), and Pearson et al. (2024). This sample of SNe Ia spans a variety of peak absolute magnitudes and early-time NIR diversity (see §5.3.3), yet despite that, the spectra are relatively similar in the +80 day to +210 day window.

We identify a mix of permitted Fe and Co blends (from the Marion et al. 2009 line list) and forbidden Fe and Co blends (from the Höflich et al. 2021 line list). Figure 12 includes these lines, denoting permitted emission with dashed lines and forbidden emission with solid lines.

The 1.25 μm and 1.55 μm features during the transition from photospheric to nebular phases are ubiquitous in SNe Ia. While +90 days is early to transition to the nebular phase in the optical, the NIR becomes nebular and shows forbidden emission lines earlier than the optical. The broad emission feature at \sim 1.25 μm is a blend of [Fe II] 1.257, 1.271, 1.279, and 1.294 μm . At 1.55 μm , the feature is likewise a blend of [Fe II] 1.534, 1.600, 1.644, and 1.677 μm . The strongest permitted features are Fe II 0.8801, 0.9998, 1.0500, 1.0863 μm and Co II 1.5759, 1.6064, 1.6361, 1.7772, 1.7462 μm (O’Hora et al. 2024).

Every SN Ia except SN 2014J shows absorption features at 0.90 μm and 1.00 μm . At first glance, this may be attributable to Mg II 0.9227 and 1.0092, respectively, but Mg II 1.0927 is the stronger feature at lower temperatures (see Table 5 in Marion et al. 2009). In the H band, the +80–100-day spectra have emission at 1.7 μm , decreasing in strength over time. Different blends of Fe/Co begin to appear after +100 days.

Finally, the K -band features are generally similar for all SNe Ia in this phase range. Longer wavelengths measure deeper into the ejecta; thus, the K band may already be optically thin and start to show blends of forbidden Fe/Co features, or there could still be permitted Co II

emission.

5. IMPLICATIONS FOR SNE Ia MODELS

The early-time observations of SN 2024epr provide helpful constraints to evaluate proposed models for SNe Ia. Below, we discuss the rising light curve morphology (§5.1), the early-time optical spectra (§5.2), and the NIR spectroscopic features at early times (§5.3).

We use these observational diagnostics to qualitatively discuss predictions made by various physical models (see sections below). While we are unable to link SN 2024epr to a single SN Ia model definitively, the high-velocity features challenge some delayed-detonation models, and we rule out He detonation models with a thick ($M_{\text{shell}} \geq 0.05M_{\odot}$) He shell from the fits to the multiband photometry (§5.1), and the apparent lack of He features in the NIR spectra (§5.3.1).

5.1. Model Implications from the Rising Light Curve

Some SNe Ia models may differ in their predictions for the shape of the rising light curve (e.g., Kasen 2010; Piro & Nakar 2013, 2014; Piro & Morozova 2016; Maeda et al. 2018; Polin et al. 2019; Magee & Maguire 2020; Maeda et al. 2023). Such differences may arise from intrinsic differences in the SN Ia progenitor scenario (e.g., companion interaction) or explosion mechanism (e.g., double detonation), or from an extrinsic effect like viewing angle. Observationally, there are three categories of early-time rising light curve: “single” power law rises in which the rising light curve is well-described by a single power law, “double” or “excess” rises, which are best described by a power law with an additional component (e.g., another power law or a Gaussian), and “bump” rising light curves which have non-monotonic light curves exhibiting a decline in flux before rising to the main light curve peak (Hoogendam et al. 2024b, and potentially correlate with negative Hubble residuals, e.g., Ye et al. 2024).

For SN 2024epr, we fit the combined rest-frame Pan-STARRS and ZTF g -band light curve with a single power-law model, masking data after \sim 10 days. Valletly et al. (2019, 2021); Fausnaugh et al. (2021) find that the choice of the fitting range of a light curve can significantly change the fit results and recommend fitting only up to 40% of the SN peak flux, which, for SN 2024epr is at \sim 10 days. Other studies (e.g., Fausnaugh et al. 2023; Hoogendam et al. 2024a, 2025) use a double power-law to fit transients through maximum light, negating this potential systematic. Despite having photometric coverage at this time, there is an offset in the Post light curves compared to those from ZTF and YSE, which have a negligible difference. This offset is likely due to differences in the filter functions, and it ultimately prevents us from using this more robust fitting technique. Thus, we opt to fit only at early times, with a model defined by

$$f(t) = \begin{cases} 0 & t < t_0 \\ a \times (x - t_0)^b & t_0 \leq t \end{cases} \quad (1)$$

where a is a multiplicative scaling factor, b is the power law index, and t_0 is the time of first light from the model. The best values from the fit are $a = 0.11 \pm 0.01$ mJy $b = 1.80 \pm 0.01$, and $t_0 = -18.9 \pm 0.3$ days, or MJD 60387.7 ± 0.3 . Figure 13 shows the data and fit.

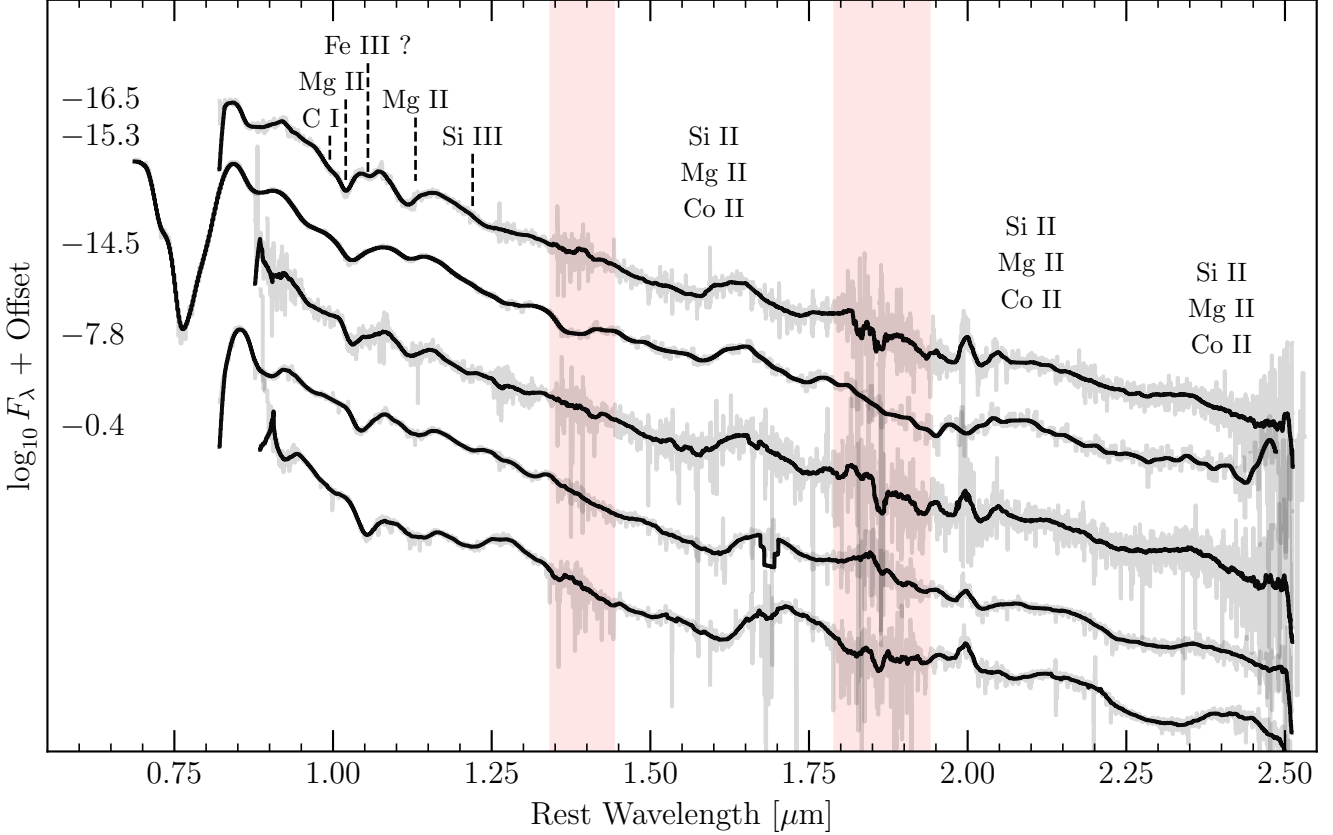


FIG. 11.— Pre-peak NIR spectroscopic time series for SN 2024epr. Light red shading denotes telluric regions.

A single power-law model fits the rising light curve in this phase range well ($\chi^2/n = 2.3$; with an additional 2% uncertainty added to the photometry to account for potential underestimation of the photometric precision). There is no trend in the residuals as a function of time. For those reasons, we do not perform a double power law or power law and Gaussian fit. Based on this simple power-law fit, the first optical and NIR spectra of SN 2024epr are $2.1 \pm 0.1/2.4 \pm 0.1$ days after first light, respectively, making them remarkably early spectra for a SN Ia. Additionally, given the constraining last non-detection from ATLAS, SN Ia models that require additional flux beyond a simple single power law at early times may not accurately match the rising light curve of SN 2024epr.

We also compare the multi-band light curves of SN 2024epr with those of He detonation models. Figure 14 shows model He detonation absolute magnitudes from Polin et al. (2019) and our Pan-STARRS *griz* photometry. Model fits are highly sensitive to the time of first light and the distance to the SN Ia, so we perform χ^2 minimization fits to determine the horizontal and vertical shifts to the model light curves to obtain the best fit for our data. Even with the phase and distance offsets (i.e., horizontal and vertical shifts to minimize the reduced χ^2 value), the Polin et al. (2019) model light curves struggle to reproduce the observed light curves.

Generally, the smaller $0.01 M_\odot$ He shells match the *griz* light curves well at 10 days before peak, but the larger $0.05 M_\odot$ He shell light curves match better at peak.

No single model light curve can explain our observed data, particularly the unusual colors near peak. Given the last non-detection from ATLAS for SN 2024epr of 18.8 mag (~ -13 absolute magnitude using the redshift-inferred distance, or ~ -13.5 mag using the distance from SN 2024epr) at ~ -21 days before maximum light, we rule out the scenarios with larger He shells ($M_{\text{shell}} \geq 0.05 M_\odot$) that would produce excess flux in the early-time observations. Thus, thinner He shells (e.g., Boos et al. 2021, 2024b), which do not produce excess flux in the rising light curve, may be preferential to thicker He shells to explain SN 2024epr and other SNe Ia with strong, high-velocity Ca features and smoothly rising light curves. This is not to suggest that SN 2024epr definitively originates from a He-detonation. Non-He-detonation models may also be able to replicate the observed properties of SN 2024epr (a thorough analysis of every model is beyond the scope of this work).

5.2. Model Implications from Early-Time Optical Spectra

There are apparent differences between extremely high-velocity SNe Ia, like SNe 2009ig, 2012fr, 2020jgl, 2021aefx, and 2024epr, and the canonically normal SNe 2011fe and 2017cbv. We find a qualitative trend between the Ca II NIR feature strength and the Si II 5972 feature strength at peak, as shown in Figure 10. SN 2009ig has the weakest Ca II NIR and Si II 5972 features, whereas SN 2024epr has the strongest Ca II NIR and Si II 5972; the other two SNe Ia have Si II 5972 and

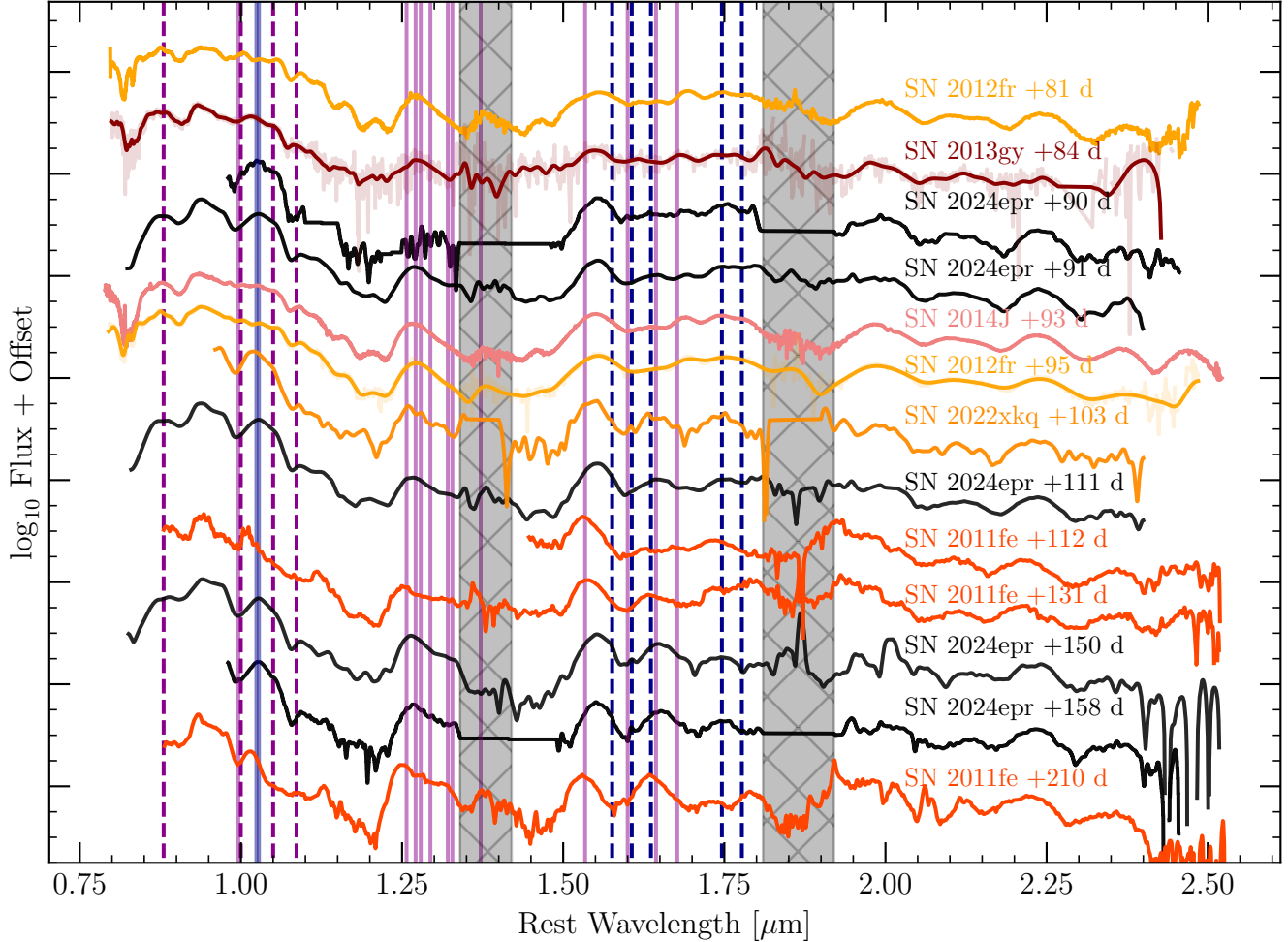


FIG. 12.— SN 2024epr compared to other SNe Ia with NIR data in the +81 to +210 days phase range. Solid lines denote forbidden Fe (magenta) and Co (blue) transitions, respectively, and dashed lines denote permitted Fe and Co transitions, respectively. Grey-shaded regions denote telluric regions.

Ca II strengths between those of SNe 2009ig and 2024epr.

The presence of Si and Ca in the outermost layers of the SN 2024epr ejecta (at $\sim 38\,000\text{ km s}^{-1}$) also has modeling implications. High-velocity Ca features may be from primordial Ca (Lentz et al. 2000), so such objects may be explosions of higher metallicity CO WDs. This would agree with the generally redder colors of SN 2020jgl (Galbany et al. 2025) and SN 2024epr (Section 3.2). Alternatively, the Ca may be the product of SN Ia nucleosynthesis; higher-density deflagration-to-detonation transitions in the delayed detonation models of Iwamoto et al. (1999) produce higher Ca velocities. The Iwamoto et al. (1999) models match the apparent lack of He and the smoothly rising light curve of SN 2024epr, but it is unclear whether they can produce Ca with a velocity of $35\,000\text{ km s}^{-1}$.

Alternatively, double detonation models may have high-velocity features, especially if the line-of-sight is aligned with the location of the He detonation (e.g., Boos et al. 2021). A thin He shell burns only to Si or Ca and could also produce high-velocity features (e.g., Moore et al. 2013; Shen & Moore 2014; Townsley et al. 2019; Gronow et al. 2020; Boos et al. 2021). This is also consistent with less line blanketing, which is predicted to occur in thick-shell double detonation models. These

models have significant line blanketing for wavelengths less than 5000 Å due to He burned to Ni in the initial detonation (e.g., Polin et al. 2019). This is inconsistent with SN 2024epr, which does not have significant flux suppression in that spectral region.

5.3. Model Implications from Early-Time NIR Spectra

5.3.1. Implications from No Obvious He Features

He may form spectral features in the optical, but potential He features would blend with stronger features typical of SNe Ia, such as S II and Si II, making them difficult to detect confidently. In the NIR, however, the strongest He features, at He I 1.083 μm and He I 2.058 μm , suffer less severe blending.

We do not observe evidence for He in our NIR spectral time series (Figure 15). For the He I 1.083 μm feature, several absorption features could be He I, but their velocities are too slow to be consistent with the outer layers of the ejecta of SN 2024epr. We would expect the early-time He velocity to be similar to Ca because it must be the most exterior ejecta layer; however, He may be optically thin at these velocities. The most likely He I feature in this wavelength region is between $20\,000\text{ km s}^{-1}$ and $10\,000\text{ km s}^{-1}$, but we do not see a similarly evolving

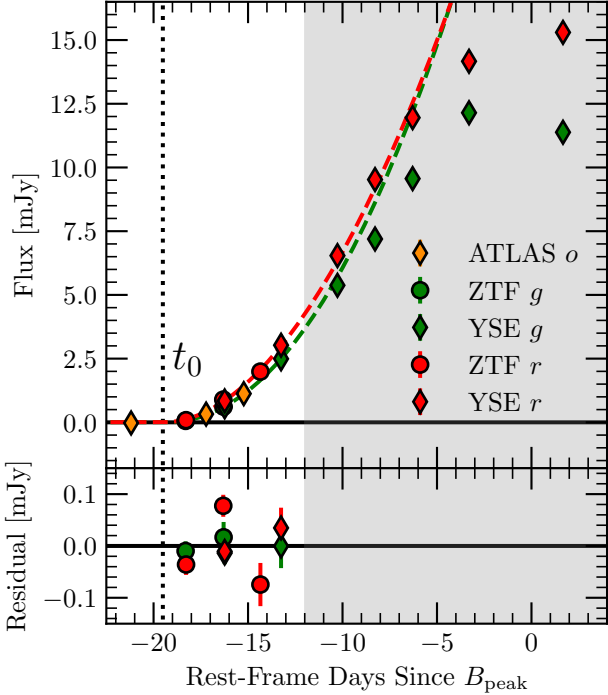


FIG. 13.— Rising light curve fits and residuals for SN 2024epr. The grey shaded region denotes the data range excluded from the fit, and the vertical dotted line denotes the time of explosion t_0 as determined from a single power law fit. *Top*: The combined YSE (diamonds) and ZTF (circles) g - and r -band light curves (green and red) and best-fit lines (dashed lines) along with ATLAS o -band data (orange diamonds). *Bottom*: Fit residuals for the single component fit.

feature in the K -band at $2.058\text{ }\mu\text{m}$. Thus, we prefer the interpretation of this “knee” feature as $\text{C I } 1.0693\text{ }\mu\text{m}$, which has been previously identified in SNe Ia (Hsiao et al. 2013; Marion et al. 2015; Hsiao et al. 2015, 2019; Pearson et al. 2024). If it is C I , this feature has a velocity of $\sim 23\,000\text{ km s}^{-1}$. While this is almost twice as fast as the C I velocity in iPTF13ebh and SN 2022xkq, it is not inconsistent since iPTF13ebh and SN 2022xkq are both low-luminosity SNe Ia with slower ejecta velocities. The detection of C I in SNe Ia has been associated with high ejecta masses and delayed detonation explosions (Höflich et al. 2002; Hsiao et al. 2015, 2019).

Double detonation models with thin (e.g., Boos et al. 2021) or thick (e.g., Collins et al. 2023) shells may have He in the outer layers of the ejecta. Thick-shell models may have enough He to produce a detectable absorption feature (Callan et al. 2024; Collins et al. 2024), which is disfavored by our observations. In contrast, the He from thin-shell models is optically thin (Boos et al. 2024a) and leaves no spectroscopic imprint. However, double-detonation models tend to have less C (e.g., Fink et al. 2010), which may be in contradiction to the NIR spectra.

5.3.2. Implications from Mg Features

Similarly to Figure 15, Figure 16 shows the velocity evolution of prominent Mg II features (the location of Mg II was determined by Hsiao et al. 2013; Marion et al. 2015; Hsiao et al. 2015 using SYNAPPS; Thomas et al. 2011a). Mg traces the extent of explosive carbon burning, and the epoch where the Mg velocity becomes con-

stant in time indicates the boundary in velocity space between explosive C and explosive O burning (Wheeler et al. 1998).

In SN 2024epr, Mg II evolves from $\sim 20\,000\text{ km s}^{-1}$ shortly after the explosion to $\sim 10\,000\text{ km s}^{-1}$ near peak. The delayed detonation models presented in Wheeler et al. (1998) have the C/O boundary at 15 000 to 16 000 km s^{-1} , which is higher than the velocity seen in SN 2024epr, especially given that our spectral time series stops at peak where the Mg II velocities may still be slowing. This suggests that the boundary between explosive C and explosive O burning is deeper in the ejecta than the Wheeler et al. (1998) delayed detonation models predict. Variations in transition density, metallically, and C/O ratio in delayed detonation models are able to produce Mg velocities more similar to those seen in SN 2024epr (Hoeflich et al. 2017; Cain et al. 2018).

5.3.3. Comparison to Other SNe Ia

We compare our NIR spectra of SN 2024epr to SN 2011fe (Hsiao et al. 2013), SN 2012fr (Lu et al. 2023), iPTF13ebh (Hsiao et al. 2015), SN 2013gy (Lu et al. 2023), SN 2017cbv (Wang et al. 2020), and SN 2022xkq (Pearson et al. 2024) in Figure 17. Our comparison sample consists of all SNe Ia whose NIR spectral time series begins 10 days before peak light and contains at least two epochs.

In the earliest SNe Ia NIR spectra, we see three different NIR behaviors: SN 2017cbv is a featureless continuum, SN 2011fe has only Mg II, and SN 2024epr has Mg II and 1.06 , and $1.12\text{ }\mu\text{m}$ features. The underlying physics driving the diversity in the early-time NIR spectral features is unclear, and a larger observational sample is needed.

There is tentative evidence that the presence of features in the NIR correlates with the luminosity of the SNe Ia themselves. The most luminous SNe in our comparison sample, SNe 2012fr and 2017cbv, have the fewest absorption features between -14 to -10 days. The other SNe Ia show at least one strong absorption feature, Mg II $1.0972\text{ }\mu\text{m}$. This Mg II feature is stronger in the subluminous iPTF13ebh and SN 2022xkq than in the normal SNe 2011fe and 2013gy. Additionally, the subluminous SNe Ia have a second absorption feature to the blue, which is claimed to be unburnt C (Hsiao et al. 2015; Pearson et al. 2024), and an additional Mg II feature observed at $\sim 1.12\text{ }\mu\text{m}$; we also claim these features are present in SN 2024epr. This trend may arise from composition or excitation differences.

The $\sim 1.12\text{ }\mu\text{m}$ Mg II feature strength also appears to depend on luminosity. This feature is seen throughout the spectral time series of iPTF13ebh, SN 2022xkq, and SN 2024epr, and it is present at maximum light, albeit with differing strengths and width, in the aforementioned SNe Ia and SNe 2011fe and 2013gy. Both SNe 2022xkq and 2024epr have a single feature centered roughly at $\sim 1.12\text{ }\mu\text{m}$, whereas iPTF13ebh has two absorption troughs, similar to the weaker troughs potentially seen in SNe 2011fe and 2013gy. SN 2017cbv shows a weak Mg II feature, whereas SN 2012fr is still featureless, even at maximum light. This trend has several potential causes, including ionization differences, variations in the outer layers from differences in the progenitor C

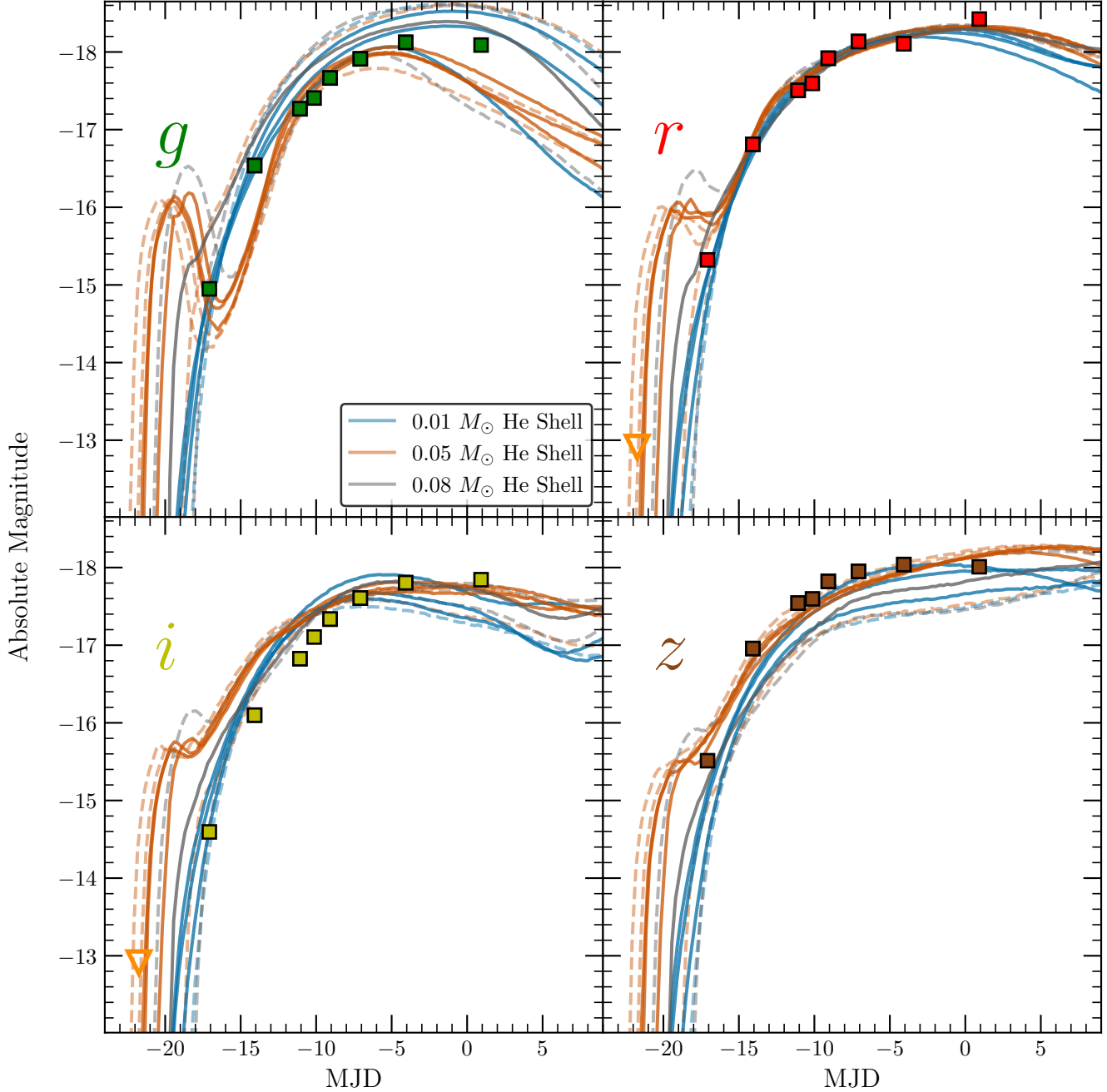


FIG. 14.— Comparison of selected He detonation model light curves from Polin et al. (2019) to our Pan-STARRS *griz*-band photometry (squares) that have the lowest reduced χ^2 values after fitting for optimal vertical (accommodating uncertainty in the redshift-derived distance) and horizontal (accommodating uncertainty in the time of peak) offsets between the model and data. The ATLAS last non-detection is shown in orange but not included in the χ^2 fitting. The models are colored by He-shell mass, with different models of the same color varying in WD mass. Solid lines denote models with $\chi^2/N \leq 6$, and dashed lines denote models with $6 < \chi^2/N \leq 9$. An additional 2% uncertainty is included in the fit uncertainties to account for the potential underestimation of photometric uncertainties.

to O ratio or metallicity, or a difference in the explosion mechanism.

Finally, the “notch” feature at $\sim 1.07 \mu\text{m}$ seen in iPTF13ebh, SN 2022xkq, and SN 2024epr at earlier times may be Fe III, which would suggest the presence of ionizing photons, and thus plausibly ^{56}Ni as well, in the outermost ejecta layers. Relative to the time of the explosion, the notch appears within approximately the first two days. Fe-group elements in the outermost layers of

the ejecta could arise from either enhanced ^{56}Ni mixing or the presence of surface ^{56}Ni (e.g., Magee et al. 2020; Magee & Maguire 2020). While not confirmed, understanding the origins of this notch feature may help constrain the extent of mixing or surface burning in SNe Ia. One caveat to this is that a high-metallicity progenitor could also have primordial Fe that produces this feature (and may naturally also explain the redder colors), and its short lifetime could be due to an ionization change

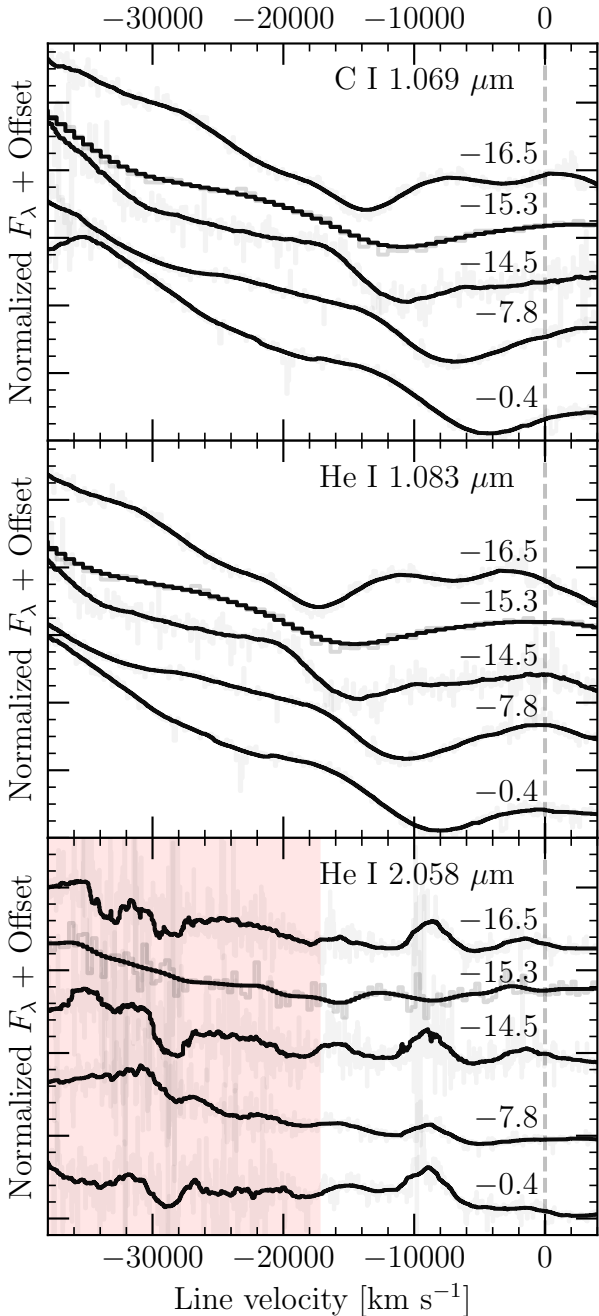


FIG. 15.— The photospheric NIR spectral evolution of SN 2024epr in regions near potential He features. *Top*: Velocities with respect to C I 1.0693 μm . *Middle*: Velocities with respect to He I 1.083 μm . *Bottom*: Velocities with respect to He I 2.058 μm . We rule out the presence of He I given the lack of an obvious feature at $\sim 2 \mu\text{m}$ to complement any feature in the 1.083 μm region. The emission feature at $\sim -10000 \text{ km s}^{-1}$ in the bottom panel is a reduction artifact and not physical. The shaded red area in the bottom panel denotes the telluric region.

rather than a surface-heavy distribution.

6. CONCLUSIONS

Our observations of SN 2024epr are some of the earliest-ever SN Ia observations, especially in the NIR. When measured in days before *B*-band maximum, only the 0.9–1.8 μm spectrum of SN 2017cbv from Wang et al.

(2020) is earlier than our first 0.8–2.5 μm spectrum of SN 2024epr. Such early-time NIR spectroscopic time series data within a couple of days of the explosion exist for only a few SNe Ia (Hsiao et al. 2013, 2015; Wang et al. 2020; Pearson et al. 2024) and are strong diagnostics of the underlying physics (see, e.g., Hsiao et al. 2019).

The early-time optical spectra show high velocity Si II $\lambda 6355$ and Ca II NIR features at speeds of $\sim 0.1c$, yet there are only photospheric velocity features by maximum light. SN 2024epr is in the “cool” region of the Branch et al. (2006) classification scheme and has the strongest Ca II NIR pEW in our comparison sample.

The early-time NIR spectra show strong Mg features at a velocity of $\sim 20000 \text{ km s}^{-1}$, and a fast-evolving C I feature at $\sim 23000 \text{ km s}^{-1}$. Despite obtaining these spectra two days after the estimated time of first light, we do not find any evidence for He features in our spectral time series. Compared to other SNe Ia with early-time NIR spectra, SN 2024epr is normal, albeit with higher Mg velocities. Generally, there is growing evidence for a diversity of early-time NIR spectra, and more early-time NIR spectra will improve our understanding of the observational and, ultimately, physical differences between SNe Ia.

The transitional phase NIR spectra show clear Fe group elements in emission (Fe II and Co II), and we tentatively propose Si III to explain the feature at 1.25 μm . We also identify what may be Ca II and Mg II features in the transitional phase spectra, suggesting that inner layers of the ejecta also undergo incomplete burning. Lastly, these later time spectra do not show evidence for H or He from a non-degenerate companion or surrounding H- or He-rich circumstellar medium.

Because our photometric coverage begins promptly after discovery, we searched for excess flux in the rising light curve of SN 2024epr. We do not find evidence for excess flux in SN 2024epr, ruling out thick He shells, which may produce excess flux at early times. We also compare the Pan-STARRS photometry to model He-detonation light curves from Polin et al. (2019), and we find that no single model fits the data well. In particular, the *i* band, which hosts the extremely strong Ca II NIR feature, tends to be fainter than the model predicts. The best-fitting double detonation models favor smaller He shells, which do not produce as much early-excess flux as larger He shells. Thin shell He donations do not burn completely to Fe group elements; instead, they produce intermediate mass elements in the outermost layers consistent with the early-time spectra of SN 2024epr. Alternatively, it may be plausible that a higher transition density between deflagration and detonation may also produce such extremely high-velocity features in a delayed detonation explosion.

Finally, we find several other SNe Ia (namely, SNe 2009ig, 2012fr, 2020jgl, and 2021aefx) also have high velocity ($v \approx 30000 \text{ km s}^{-1}$) intermediate mass elements shortly after explosion. Given the paucity of SNe Ia with prompt spectroscopic observations after the explosion and that these objects all evolve to be consistent with normal SNe Ia at peak light, a significant fraction of SNe Ia potentially may have unobserved high-velocity features at early times, which require prompt discovery and rapid spectroscopic classification to reveal.

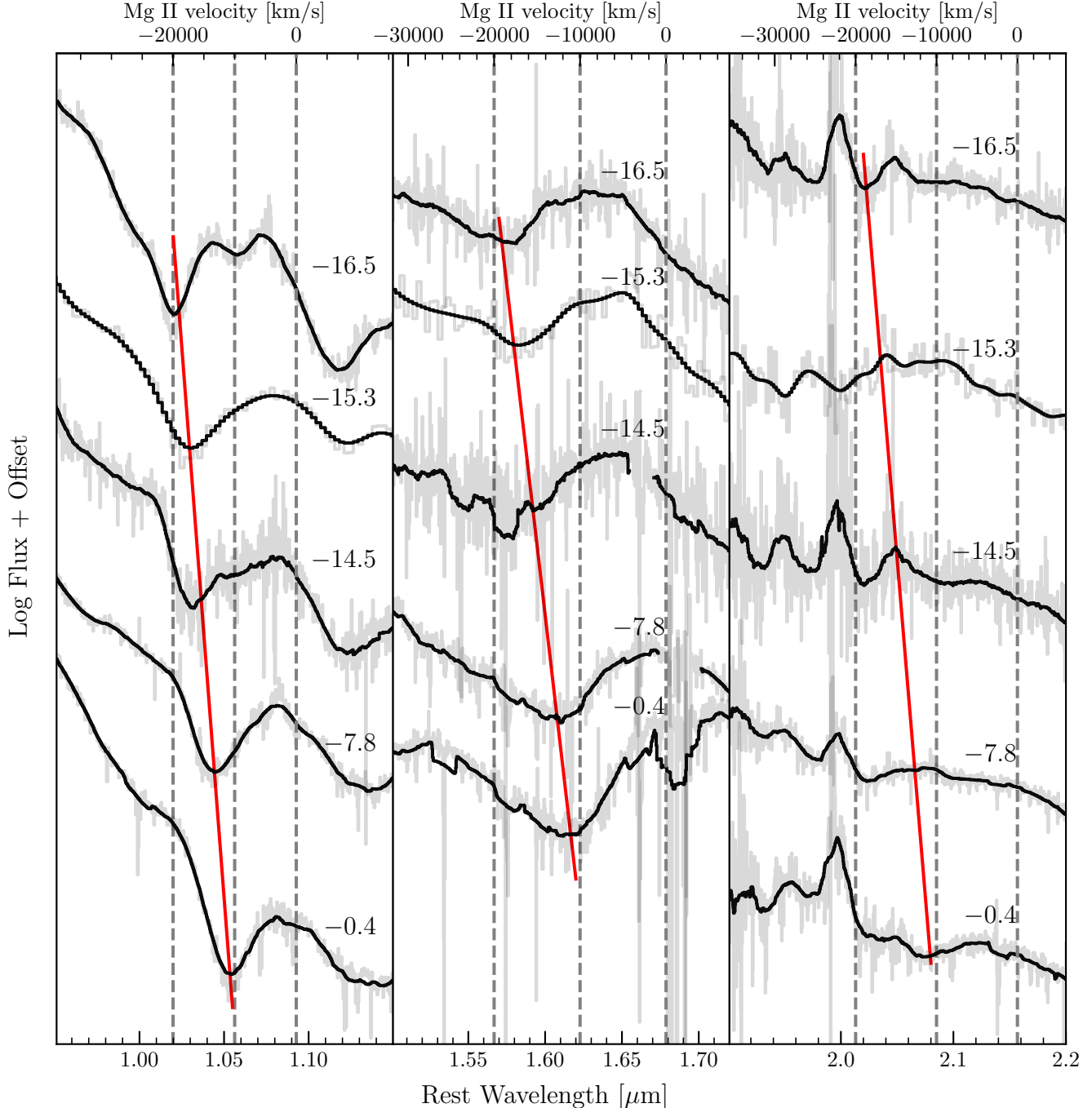


FIG. 16.— The velocity evolution of Mg II NIR spectral features in SN 2024epr. The fiducial red line is to guide the eye along the velocity evolution of the Mg II features and is not physically meaningful. The dashed grey lines indicate Mg II velocities of 20 000, 10 000, and 0 km s⁻¹, respectively.

We find evidence for several trends in the early-time behavior of SNe Ia. First, SNe Ia with high-velocity features at early times generally evolve to be normal SNe Ia at peak. Second, the substantial NIR diversity between SNe Ia at early times is also seen at maximum light, contrasting the optical where most early-time differences between SNe Ia become less stark near maximum light. This work highlights the utility of early-time optical and NIR observations to probe the composition of the outermost ejecta layers most sensitive to differences in the

progenitor scenario and/or explosion mechanism, making it essential to grow the sample of SNe Ia with early-time data to understand their explosive origins better.

ACKNOWLEDGMENTS

We thank the anonymous referee for providing helpful feedback that improved this manuscript. We thank Sahana Kumar, Jing Lu, Abigail Polin, Ken Shen, Eddie Baron, and Peter Hoeflich for their helpful discussions. This material is based upon work supported by the

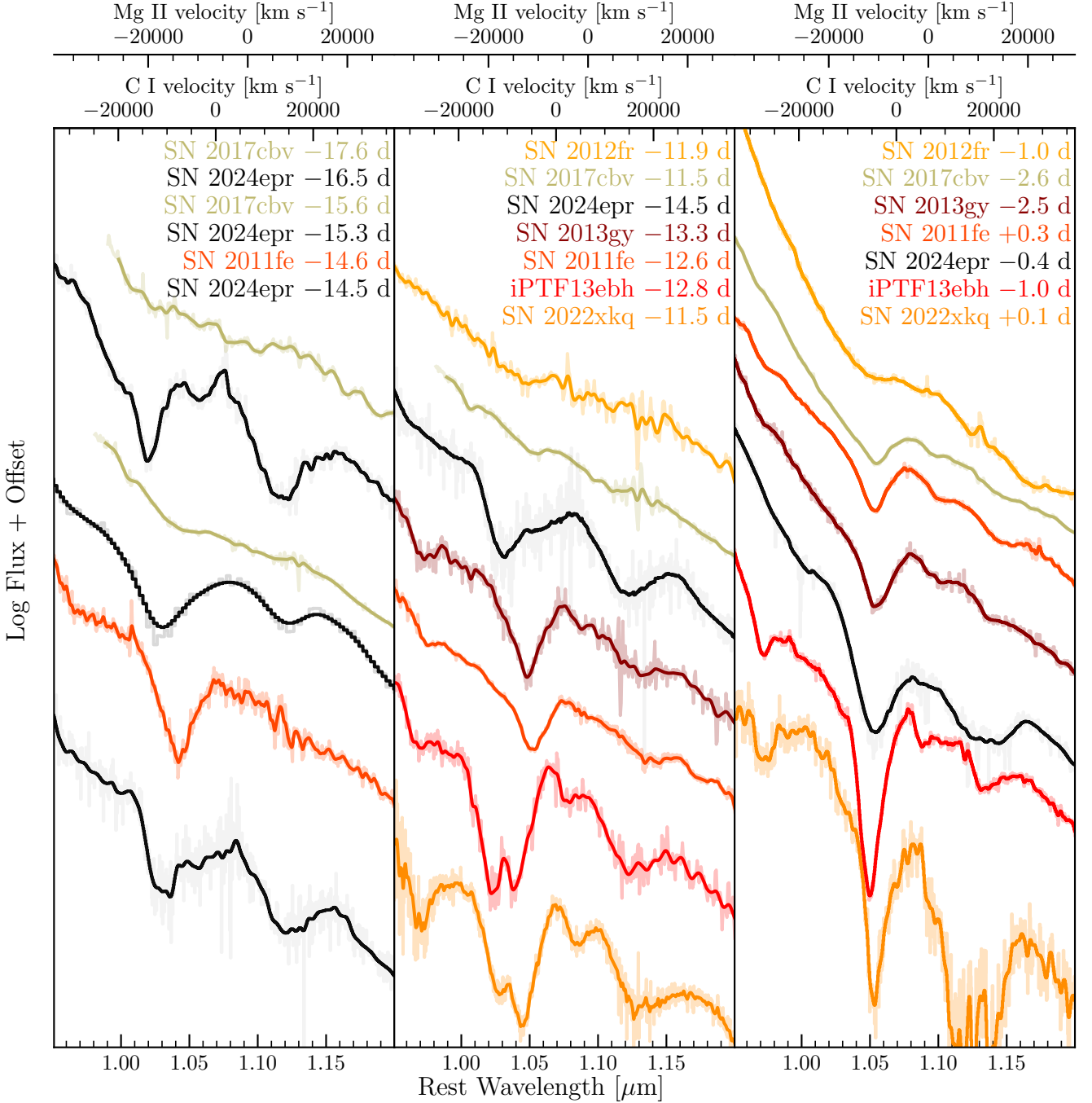


FIG. 17.— Comparison of other early-time NIR spectra to other SNe Ia with early-time NIR spectra.

National Science Foundation Graduate Research Fellowship Program under Grant Nos. 1842402 and 2236415. Any opinions, findings, conclusions, or recommendations expressed in this material are those of the authors and do not necessarily reflect the views of the National Science Foundation. D.O.J. acknowledges support from NSF grants AST-2407632 and AST-2429450, NASA grant 80NSSC24M0023, and HST/JWST grants HST-GO-17128.028, HST-GO-16269.012, and JWST-GO-05324.031, awarded by the Space Telescope Science Institute (STScI), which is operated by the Association of Universities for Research in Astronomy, Inc., for NASA,

under contract NAS5-26555. The Shappee group at the University of Hawai'i is supported with funds from NSF (grants AST-1908952, AST-1911074, & AST-1920392) and NASA (grants HST-GO-17087, 80NSSC24K0521, 80NSSC24K0490, 80NSSC24K0508, 80NSSC23K0058, & 80NSSC23K1431). The UCSC team is supported in part by NASA grants 80NSSC23K0301 and 80NSSC24K1411; and a fellowship from the David and Lucile Packard Foundation to R.J.F. A.D. is supported by the European Research Council (ERC) under the European Union's Horizon 2020 research and innovation programme (Grant Agreement No. 101002652). A.R.W. is supported by

funding through AST-2421845 and funding from the Simons Foundation for the NSF-Simons SkAI Institute, the LSST Discovery Alliance through the LINCC Incubator Program and the Catalyst Program, supported in part by Wasabi Technologies, the US DOE through the Department of Physics at the University of Illinois, Urbana-Champaign (# 13771275), and the 2024 DOE SCGSCR program and Lawrence Berkeley National Laboratory. This work is supported by the National Science Foundation under Cooperative Agreement PHY-2019786 (The NSF AI Institute for Artificial Intelligence and Fundamental Interactions, <http://iaifi.org/>).

This work was supported by National Aeronautics and Space Administration (NASA) Keck PI Data Awards, administered by the NASA Exoplanet Science Institute.

Observations from coauthor S.A.S. were made with undergraduates in the spring 2024 Astronomy 331 course at Sonoma State University. These observations were made under the aegis of the ASTRAL (Astronomy/STEM Alliance with Lick) consortium, supported by a generous grant from the Gordon and Betty Moore Foundation (PI: B. Macintosh).

The Young Supernova Experiment (YSE) and its research infrastructure is supported by the European Research Council under the European Union’s Horizon 2020 research and innovation programme (ERC Grant Agreement 101002652, PI K. Mandel), the Heising-Simons Foundation (2018-0913, PI R. Foley; 2018-0911, PI R. Margutti), NASA (NNG17PX03C, PI R. Foley), NSF (AST-1720756, AST-1815935, PI R. Foley; AST-1909796, AST-1944985, PI R. Margutti), the David & Lucille Packard Foundation (PI R. Foley), VILLUM FONDEN (project 16599, PI J. Hjorth), and the Center for AstroPhysical Surveys (CAPS) at the National Center for Supercomputing Applications (NCSA) and the University of Illinois Urbana-Champaign. Pan-STARRS is a project of the Institute for Astronomy of the University of Hawaii, and is supported by the NASA SSO Near Earth Observation Program under grants 80NSSC18K0971, NNX14AM74G, NNX12AR65G, NNX13AQ47G, NNX08AR22G, 80NSSC21K1572, and by the State of Hawaii. The Pan-STARRS1 Surveys (PS1) and the PS1 public science archive have been made possible through contributions by the Institute for Astronomy, the University of Hawaii, the Pan-STARRS Project Office, the Max-Planck Society and its participating institutes, the Max Planck Institute for Astronomy, Heidelberg and the Max Planck Institute for Extraterrestrial Physics, Garching, The Johns Hopkins University, Durham University, the University of Edinburgh, the Queen’s University Belfast, the Harvard-Smithsonian Center for Astrophysics, the Las Cumbres Observatory Global Telescope Network Incorporated, the National Central University of Taiwan, STScI, NASA under grant NNX08AR22G issued through the Planetary Science Division of the NASA Science Mission Directorate, NSF grant AST-1238877, the University of Maryland, Eotvos Lorand University (ELTE), the Los Alamos National Laboratory, and the Gordon and Betty Moore Foundation.

Based on observations obtained at the international Gemini Observatory, a program of NSF NOIRLab, which is managed by the Association of Universities for Research in Astronomy (AURA) under a cooperative agree-

ment with the U.S. National Science Foundation on behalf of the Gemini Observatory partnership: the U.S. National Science Foundation (United States), National Research Council (Canada), Agencia Nacional de Investigación y Desarrollo (Chile), Ministerio de Ciencia, Tecnología e Innovación (Argentina), Ministério da Ciência, Tecnologia, Inovações e Comunicações (Brazil), and Korea Astronomy and Space Science Institute (Republic of Korea). Data were taken by programs GN-2024A-Q-136, GN-2024A-Q-226, and GN-2024B-Q-109. This work was enabled by observations made from the Gemini North telescope, located within the Maunakea Science Reserve and adjacent to the summit of Maunakea. We are grateful for the privilege of observing the Universe from a place that is unique in both its astronomical quality and its cultural significance.

Some of the data presented herein were obtained at Keck Observatory, which is a private 501(c)3 non-profit organization operated as a scientific partnership among the California Institute of Technology, the University of California, and the National Aeronautics and Space Administration. The Observatory was made possible by the generous financial support of the W. M. Keck Foundation. The authors wish to recognize and acknowledge the very significant cultural role and reverence that the summit of Maunakea has always had within the indigenous Hawaiian community. We are most fortunate to have the opportunity to conduct observations from this mountain.

The Infrared Telescope Facility, which is operated by the University of Hawaii under contract 80HQTR24DA010 with the National Aeronautics and Space Administration.

A major upgrade of the Kast spectrograph on the Shane 3 m telescope at Lick Observatory was made possible through generous gifts from the Heising-Simons Foundation as well as William and Marina Kast. Research at Lick Observatory is partially supported by a generous gift from Google.

UKIRT is owned by the University of Hawaii (UH) and operated by the UH Institute for Astronomy.

This work has made use of data from the Asteroid Terrestrial-impact Last Alert System (ATLAS) project. The Asteroid Terrestrial-impact Last Alert System (ATLAS) project is primarily funded to search for near earth asteroids through NASA grants NN12AR55G, 80NSSC18K0284, and 80NSSC18K1575; byproducts of the NEO search include images and catalogs from the survey area. This work was partially funded by Kepler/K2 grant J1944/80NSSC19K0112 and HST GO-15889, and STFC grants ST/T000198/1 and ST/S006109/1. The ATLAS science products have been made possible through the contributions of the University of Hawaii Institute for Astronomy, the Queen’s University Belfast, the Space Telescope Science Institute, the South African Astronomical Observatory, and The Millennium Institute of Astrophysics (MAS), Chile.

Based on observations obtained with the Samuel Oschin Telescope 48-inch and the 60-inch Telescope at the Palomar Observatory as part of the Zwicky Transient Facility project. ZTF is supported by the National Science Foundation under Grant Nos. AST-1440341, AST-2034437, and a collaboration including Caltech, IPAC, the Weizmann Institute for Science, the Oskar Klein Center at Stockholm University, the University

of Maryland, the University of Washington, Deutsches Elektronen-Synchrotron and Humboldt University, the TANGO Consortium of Taiwan, the University of Wisconsin at Milwaukee, Trinity College Dublin, Lawrence Livermore National Laboratories, and IN2P3, France. Operations are conducted by COO, IPAC, and UW.

YSE-PZ was developed by the UC Santa Cruz Transients Team, supported in part by NASA grants NNG17PX03C, 80NSSC19K1386, and 80NSSC20K0953; NSF grants AST-1518052, AST-1815935, and AST-

1911206; the Gordon & Betty Moore Foundation; the Heising-Simons Foundation; a fellowship from the David and Lucile Packard Foundation to R. J. Foley; Gordon and Betty Moore Foundation postdoctoral fellowships and a NASA Einstein fellowship, as administered through the NASA Hubble Fellowship program and grant HST-HF2-51462.001, to D. O. Jones; and a National Science Foundation Graduate Research Fellowship, administered through grant No. DGE-1339067, to D. A. Coulter.

REFERENCES

Aleo P. D., et al., 2023, *ApJS*, **266**, 9
 Ashall C., et al., 2019a, *ApJ*, **875**, L14
 Ashall C., et al., 2019b, *ApJ*, **878**, 86
 Ashall C., et al., 2021, *ApJ*, **922**, 205
 Ashall C., et al., 2022, *ApJ*, **932**, L2
 Aznar-Siguán G., García-Berro E., Lorén-Aguilar P., Soker N., Kashi A., 2015, *MNRAS*, **450**, 2948
 Bellm E. C., et al., 2019, *PASP*, **131**, 018002
 Benetti S., et al., 2004, *MNRAS*, **348**, 261
 Benetti S., et al., 2005, *ApJ*, **623**, 1011
 Blondin S., et al., 2012, *AJ*, **143**, 126
 Blondin S., Dessart L., Hillier D. J., Khokhlov A. M., 2013, *MNRAS*, **429**, 2127
 Boos S. J., Townsley D. M., Shen K. J., Caldwell S., Miles B. J., 2021, *ApJ*, **919**, 126
 Boos S. J., Dessart L., Shen K. J., Townsley D. M., 2024a, *arXiv e-prints*, p. [arXiv:2410.22276](https://arxiv.org/abs/2410.22276)
 Boos S. J., Townsley D. M., Shen K. J., 2024b, *ApJ*, **972**, 200
 Branch D., et al., 2006, *PASP*, **118**, 560
 Brout D., et al., 2022, *ApJ*, **938**, 111
 Brown P. J., Breeveld A. A., Holland S., Kuin P., Pritchard T., 2014, *Ap&SS*, **354**, 89
 Burns C. R., et al., 2011, *AJ*, **141**, 19
 Burns C. R., et al., 2014, *ApJ*, **789**, 32
 Burns C. R., et al., 2018, *ApJ*, **869**, 56
 Cain C., et al., 2018, *ApJ*, **869**, 162
 Callan F. P., et al., 2024, *arXiv e-prints*, p. [arXiv:2408.03048](https://arxiv.org/abs/2408.03048)
 Casali M., et al., 2007, *A&A*, **467**, 777
 Chambers K. C., et al., 2016, *arXiv e-prints*, p. [arXiv:1612.05560](https://arxiv.org/abs/1612.05560)
 Chandrasekhar S., 1931, *ApJ*, **74**, 81
 Childress M. J., et al., 2013, *ApJ*, **770**, 29
 Collins C. E., Sim S. A., Shingles L. J., Gronow S., Röpke F. K., Pakmor R., Seitenzahl I. R., Kromer M., 2023, *MNRAS*, **524**, 4447
 Collins C. E., et al., 2024, *arXiv e-prints*, p. [arXiv:2411.11643](https://arxiv.org/abs/2411.11643)
 Coulter D. A., et al., 2022, YSE-PZ: An Open-source Target and Observation Management System, [doi:10.5281/zenodo.7278430](https://doi.org/10.5281/zenodo.7278430)
 Coulter D. A., et al., 2023, *PASP*, **135**, 064501
 Cushing M. C., Vacca W. D., Rayner J. T., 2004, *PASP*, **116**, 362
 DerKacy J. M., Baron E., Branch D., Hoeflich P., Hauschildt P., Brown P. J., Wang L., 2020, *ApJ*, **901**, 86
 Desai D. D., et al., 2024, *MNRAS*, **530**, 5016
 Do A., et al., 2025, *MNRAS*, **536**, 624
 Elias J. H., Rodgers B., Joyce R. R., Lazio M., Doppmann G., Winge C., Rodríguez-Ardila A., 2006a, in McLean I. S., Iye M., eds, Society of Photo-Optical Instrumentation Engineers (SPIE) Conference Series Vol. 6269, Ground-based and Airborne Instrumentation for Astronomy. p. 626914, [doi:10.1117/12.671765](https://doi.org/10.1117/12.671765)
 Elias J. H., Joyce R. R., Liang M., Muller G. P., Hileman E. A., George J. R., 2006b, in McLean I. S., Iye M., eds, Society of Photo-Optical Instrumentation Engineers (SPIE) Conference Series Vol. 6269, Ground-based and Airborne Instrumentation for Astronomy. p. 62694C, [doi:10.1117/12.671817](https://doi.org/10.1117/12.671817)
 Fausnaugh M. M., et al., 2021, *ApJ*, **908**, 51
 Fausnaugh M. M., et al., 2023, *arXiv e-prints*, p. [arXiv:2307.11815](https://arxiv.org/abs/2307.11815)
 Fink M., Röpke F. K., Hillebrandt W., Seitenzahl I. R., Sim S. A., Kromer M., 2010, *A&A*, **514**, A53
 Fink M., et al., 2014, *MNRAS*, **438**, 1762
 Flewelling H. A., et al., 2020, *ApJS*, **251**, 7
 Folatelli G., et al., 2013, *ApJ*, **773**, 53
 Foley R. J., Narayan G., Challis P. J., Filippenko A. V., Kirshner R. P., Silverman J. M., Steele T. N., 2010, *ApJ*, **708**, 1748
 Foley R. J., et al., 2012, *ApJ*, **744**, 38
 Foley R. J., et al., 2018, *MNRAS*, **475**, 193
 Friesen B., Baron E., Wisniewski J. P., Parrent J. T., Thomas R. C., Miller T. R., Marion G. H., 2014, *ApJ*, **792**, 120
 Fukugita M., Ichikawa T., Gunn J. E., Doi M., Shimasaku K., Schneider D. P., 1996, *AJ*, **111**, 1748
 Galbany L., et al., 2025, *arXiv e-prints*, p. [arXiv:2501.19108](https://arxiv.org/abs/2501.19108)
 Gall E. E. E., Taubenberger S., Kromer M., Sim S. A., Benetti S., Blanc G., Elias-Rosa N., Hillebrandt W., 2012, *MNRAS*, **427**, 994
 Ganeshalingam M., et al., 2010, *ApJS*, **190**, 418
 Gerardy C. L., et al., 2004, *ApJ*, **607**, 391
 Gronow S., Collins C., Ohlmann S. T., Pakmor R., Kromer M., Seitenzahl I. R., Sim S. A., Röpke F. K., 2020, *A&A*, **635**, A169
 Hachinger S., Mazzali P. A., Tanaka M., Hillebrandt W., Benetti S., 2008, *MNRAS*, **389**, 1087
 Harvey L., et al., 2025, *arXiv e-prints*, p. [arXiv:2502.04448](https://arxiv.org/abs/2502.04448)
 Hickin M., et al., 2009, *ApJ*, **700**, 331
 Hirst P., Cardenes R., 2017, in Lorente N. P. F., Shortridge K., Wayth R., eds, Astronomical Society of the Pacific Conference Series Vol. 512, Astronomical Data Analysis Software and Systems XXV. p. 53
 Hodgkin S. T., Irwin M. J., Hewett P. C., Warren S. J., 2009, *MNRAS*, **394**, 675
 Hoeflich P., Khokhlov A., 1996, *ApJ*, **457**, 500
 Hoeflich P., Khokhlov A. M., Wheeler J. C., 1995, *ApJ*, **444**, 831
 Hoeflich P., et al., 2017, *ApJ*, **846**, 58
 Hoeflich P., et al., 2021, *ApJ*, **922**, 186
 Höflich P., Gerardy C. L., Fesen R. A., Sakai S., 2002, *ApJ*, **568**, 791
 Holmbo S., et al., 2023, *A&A*, **675**, A83
 Holoien T. W. S., et al., 2017a, *MNRAS*, **464**, 2672
 Holoien T. W. S., et al., 2017b, *MNRAS*, **467**, 1098
 Holoien T. W. S., et al., 2017c, *MNRAS*, **471**, 4966
 Holoien T. W. S., et al., 2019, *MNRAS*, **484**, 1899
 Hoogendam W. B., et al., 2022, *ApJ*, **928**, 103
 Hoogendam W. B., et al., 2024a, *MNRAS*, **530**, 4501
 Hoogendam W. B., Shappee B. J., Brown P. J., Tucker M. A., Ashall C., Piro A. L., 2024b, *ApJ*, **966**, 139
 Hoogendam W. B., et al., 2025, *ApJ*, **988**, 209
 Hosseinzadeh G., et al., 2017, *ApJ*, **845**, L11
 Hosseinzadeh G., et al., 2022, *ApJ*, **933**, L45
 Hoyle F., Fowler W. A., 1960, *ApJ*, **132**, 565
 Hsiao E. Y., et al., 2013, *ApJ*, **766**, 72
 Hsiao E. Y., et al., 2015, *A&A*, **578**, A9
 Hsiao E. Y., et al., 2019, *PASP*, **131**, 014002
 Huchra J. P., Vogeley M. S., Geller M. J., 1999, *ApJS*, **121**, 287
 Iben I. J., Tutukov A. V., 1984, *ApJS*, **54**, 335
 Ilkov M., Soker N., 2013, *MNRAS*, **428**, 579
 Iwamoto K., Brachwitz F., Nomoto K., Kishimoto N., Umeda H., Hix W. R., Thielemann F.-K., 1999, *ApJS*, **125**, 439
 Jha S. W., Maguire K., Sullivan M., 2019, *Nature Astronomy*, **3**, 706
 Johnson B. D., Leja J., Conroy C., Speagle J. S., 2021, *ApJS*, **254**, 22
 Jones D. O., et al., 2019, *ApJ*, **881**, 19
 Jones D. O., et al., 2021, *ApJ*, **908**, 143
 Jones D. O., et al., 2022, *ApJ*, **933**, 172
 Jones D. O., et al., 2024, *arXiv e-prints*, p. [arXiv:2410.17322](https://arxiv.org/abs/2410.17322)
 Karambelkar V., et al., 2024, Transient Name Server AstroNote, **81**, 1
 Kasen D., 2010, *ApJ*, **708**, 1025
 Kasen D., Röpke F. K., Woosley S. E., 2009, *Nature*, **460**, 869
 Kashi A., Soker N., 2011, *MNRAS*, **417**, 1466
 Kato M., Saio H., Hachisu I., 2018, *ApJ*, **863**, 125
 Kenworthy W. D., et al., 2021, *ApJ*, **923**, 265
 Khokhlov A. M., 1991, *A&A*, **245**, 114
 Krisciunas K., et al., 2017, *AJ*, **154**, 211
 Kromer M., et al., 2013, *ApJ*, **778**, L18
 Kromer M., et al., 2016, *MNRAS*, **459**, 4428
 Kushnir D., Katz B., Dong S., Livne E., Fernández R., 2013, *ApJ*, **778**, L37
 Lantz B., et al., 2004, in Mazuray L., Rogers P. J., Wartmann R., eds, Society of Photo-Optical Instrumentation Engineers (SPIE) Conference Series Vol. 5249, Optical Design and Engineering. pp 146–155, [doi:10.1117/12.512493](https://doi.org/10.1117/12.512493)
 Lavaux G., Hudson M. J., 2011, *MNRAS*, **416**, 2840

Leja J., Carnall A. C., Johnson B. D., Conroy C., Speagle J. S., 2019, [ApJ](#), **876**, 3

Lentz E. J., Baron E., Branch D., Hauschildt P. H., Nugent P. E., 2000, [ApJ](#), **530**, 966

Liu Z.-W., Röpke F. K., Han Z., 2023, [Research in Astronomy and Astrophysics](#), **23**, 082001

Livne E., 1990, [ApJ](#), **354**, L53

Lu J., et al., 2021, [ApJ](#), **920**, 107

Lu J., et al., 2023, [ApJ](#), **948**, 27

Maeda K., Jiang J.-a., Shigeyama T., Doi M., 2018, [ApJ](#), **861**, 78

Maeda K., Jiang J.-a., Doi M., Kawabata M., Shigeyama T., 2023, [MNRAS](#), **521**, 1897

Magee M. R., Maguire K., 2020, [A&A](#), **642**, A189

Magee M. R., Maguire K., Kotak R., Sim S. A., Gillanders J. H., Prentice S. J., Skillen K., 2020, [A&A](#), **634**, A37

Magnier E. A., et al., 2020, [ApJS](#), **251**, 6

Maoz D., Mannucci F., Nelemans G., 2014, [ARA&A](#), **52**, 107

Marion G. H., Höflich P., Gerardy C. L., Vacca W. D., Wheeler J. C., Robinson E. L., 2009, [AJ](#), **138**, 727

Marion G. H., et al., 2015, [ApJ](#), **798**, 39

Masci F. J., et al., 2019, [PASP](#), **131**, 018003

Matteucci F., Recchi S., 2001, [ApJ](#), **558**, 351

Mazzali P. A., et al., 2005, [ApJ](#), **623**, L37

McGurk R. C., Matuszewski M., Neill J. D., Martin C., Bertz R., Rockosi C., Kassis M. F., 2024, in Bryant J. J., Motohara K., Vernet J. R. D., eds, Society of Photo-Optical Instrumentation Engineers (SPIE) Conference Series Vol. 13096, Ground-based and Airborne Instrumentation for Astronomy X. p. 1309647, doi:10.1117/12.3020646

Miller J. S., Stone R. P. S., 1994, The KAST Double Spectrograph. Lick Observatory Technical Report, 66 edn

Moore K., Townsley D. M., Bildsten L., 2013, [ApJ](#), **776**, 97

Morrell N., et al., 2024, [ApJ](#), **967**, 20

Morrissey P., et al., 2018, [ApJ](#), **864**, 93

Müller-Bravo T. E., et al., 2025, arXiv e-prints, p. arXiv:2504.05856

Mulligan B. W., Zhang K., Wheeler J. C., 2019, [MNRAS](#), **484**, 4785

Neumann K. D., et al., 2023, [MNRAS](#), **520**, 4356

Noebauer U. M., Taubenberger S., Blinnikov S., Sorokina E., Hillebrandt W., 2016, [MNRAS](#), **463**, 2972

Nomoto K., 1980, in Wheeler J. C., ed., Texas Workshop on Type I Supernovae. pp 164–181

Nomoto K., 1982a, [ApJ](#), **253**, 798

Nomoto K., 1982b, [ApJ](#), **257**, 780

Nomoto K., Thielemann F. K., Yokoi K., 1984, [ApJ](#), **286**, 644

Nomoto K., Iwamoto K., Nakasato N., Thielemann F. K., Brachwitz F., Tsujimoto T., Kubo Y., Kishimoto N., 1997, [Nucl. Phys. A](#), **621**, 467

Nugent P., Phillips M., Baron E., Branch D., Hauschildt P., 1995, [ApJ](#), **455**, L147

Nugent P. E., et al., 2011, [Nature](#), **480**, 344

O'Hora J., et al., 2024, arXiv e-prints, p. arXiv:2412.09352

Pakmor R., Kromer M., Röpke F. K., Sim S. A., Ruiter A. J., Hillebrandt W., 2010, [Nature](#), **463**, 61

Pakmor R., Kromer M., Taubenberger S., Sim S. A., Röpke F. K., Hillebrandt W., 2012, [ApJ](#), **747**, L10

Pakmor R., Kromer M., Taubenberger S., Springel V., 2013, [ApJ](#), **770**, L8

Pearson J., et al., 2024, [ApJ](#), **960**, 29

Pejcha O., Antognini J. M., Shappee B. J., Thompson T. A., 2013, [MNRAS](#), **435**, 943

Pereira R., et al., 2013, [A&A](#), **554**, A27

Perlmutter S., et al., 1999, [ApJ](#), **517**, 565

Peterson E. R., et al., 2022, [ApJ](#), **938**, 112

Peterson E. R., et al., 2023, [MNRAS](#), **522**, 2478

Phillips M. M., 1993, [ApJ](#), **413**, L105

Phillips M. M., et al., 2019, [PASP](#), **131**, 014001

Piersanti L., Gagliardi S., Iben Icko J., Tornambé A., 2003, [ApJ](#), **598**, 1229

Piro A. L., Morozova V. S., 2016, [ApJ](#), **826**, 96

Piro A. L., Nakar E., 2013, [ApJ](#), **769**, 67

Piro A. L., Nakar E., 2014, [ApJ](#), **784**, 85

Polin A., Nugent P., Kasen D., 2019, [ApJ](#), **873**, 84

Prochaska J., et al., 2020a, [The Journal of Open Source Software](#), **5**, 2308

Prochaska J. X., et al., 2020b, [Journal of Open Source Software](#), **5**, 2308

Raiteri C. M., Villata M., Navarro J. F., 1996, [A&A](#), **315**, 105

Raskin C., Timmes F. X., Scannapieco E., Diehl S., Fryer C., 2009, [MNRAS](#), **399**, L156

Rayner J. T., Toomey D. W., Onaka P. M., Denault A. J., Stahlberger W. E., Vacca W. D., Cushing M. C., Wang S., 2003, [PASP](#), **115**, 362

Rest A., et al., 2005, [ApJ](#), **634**, 1103

Riess A. G., et al., 1998, [AJ](#), **116**, 1009

Riess A. G., et al., 2022, [ApJ](#), **934**, L7

Röpke F. K., Niemeyer J. C., 2007, [A&A](#), **464**, 683

Rosswog S., Kasen D., Guillotin J., Ramirez-Ruiz E., 2009, [ApJ](#), **705**, L128

Sand D. J., et al., 2016, [ApJ](#), **822**, L16

Scalzo R. A., et al., 2010, [ApJ](#), **713**, 1073

Schechter P. L., Mateo M., Saha A., 1993, [PASP](#), **105**, 1342

Schlafly E. F., Finkbeiner D. P., 2011, [ApJ](#), **737**, 103

Scolnic D., et al., 2022, [ApJ](#), **938**, 113

Seitenzahl I. R., et al., 2013, [MNRAS](#), **429**, 1156

Shen K. J., Moore K., 2014, [ApJ](#), **797**, 46

Shen K. J., Kasen D., Weinberg N. N., Bildsten L., Scannapieco E., 2010, [ApJ](#), **715**, 767

Shen K. J., Kasen D., Miles B. J., Townsley D. M., 2018, [ApJ](#), **854**, 52

Shen K. J., Boos S. J., Townsley D. M., 2024, [ApJ](#), **975**, 127

Shingles L., et al., 2021, Transient Name Server AstroNote, **7**, 1

Siebert M. R., Dimitriadis G., Polin A., Foley R. J., 2020, [ApJ](#), **900**, L27

Skrutskie M. F., et al., 2006, [AJ](#), **131**, 1163

Smith K. W., et al., 2020, [PASP](#), **132**, 085002

Sollerman J., 2024a, Transient Name Server Discovery Report, **2024-746**, 1

Sollerman J., 2024b, Transient Name Server Classification Report, **2024-779**, 1

Tanaka M., Mazzali P. A., Maeda K., Nomoto K., 2006, [ApJ](#), **645**, 470

Taylor G., et al., 2023, [MNRAS](#), **520**, 5209

Thielemann F. K., Nomoto K., Yokoi K., 1986, [A&A](#), **158**, 17

Thomas R. C., Nugent P. E., Meza J. C., 2011a, [PASP](#), **123**, 237

Thomas R. C., et al., 2011b, [ApJ](#), **743**, 27

Thompson T. A., 2011, [ApJ](#), **741**, 82

Tinyanont S., et al., 2024, [PASP](#), **136**, 014201

Tonry J. L., et al., 2018, [PASP](#), **130**, 064505

Townsley D. M., Miles B. J., Shen K. J., Kasen D., 2019, [ApJ](#), **878**, L38

Tucker M. A., 2025, [MNRAS](#), **538**, L1

Tucker M. A., et al., 2020, [MNRAS](#), **493**, 1044

Tucker M. A., et al., 2022, [PASP](#), **134**, 124502

Valley P. J., et al., 2019, [MNRAS](#), **487**, 2372

Valley P. J., Kochanek C. S., Stanek K. Z., Fausnaugh M., Shappee B. J., 2021, [MNRAS](#), **500**, 5639

Wang X., et al., 2009, [ApJ](#), **699**, L139

Wang L., et al., 2020, [ApJ](#), **904**, 14

Wang B., Leja J., Villar V. A., Speagle J. S., 2023, [ApJ](#), **952**, L10

Webbink R. F., 1984, [ApJ](#), **277**, 355

Wheeler J. C., Höflich P., Harkness R. P., Spyromilio J., 1998, [ApJ](#), **496**, 908

Whelan J., Iben Icko J., 1973, [ApJ](#), **186**, 1007

Wilson J. C., et al., 2004, in Moorwood A. F. M., Iye M., eds, Society of Photo-Optical Instrumentation Engineers (SPIE) Conference Series Vol. 5492, Ground-based Instrumentation for Astronomy. pp 1295–1305, doi:10.1117/12.550925

Woosey S. E., Kasen D., 2011, [ApJ](#), **734**, 38

Woosey S. E., Weaver T. A., 1994, [ApJ](#), **423**, 371

Wright E. L., et al., 2010, [AJ](#), **140**, 1868

Wyatt S. D., et al., 2021, [ApJ](#), **914**, 57

Ye C., Jones D. O., Hoogendoorn W. B., Shappee B. J., Dhawan S., Sharief S. N., 2024, [ApJ](#), **974**, 164

York D. G., et al., 2000, [AJ](#), **120**, 1579

de Vaucouleurs G., de Vaucouleurs A., Corwin Herold G. J., Buta R. J., Paturel G., Fouque P., 1991, Third Reference Catalogue of Bright Galaxies

van Kerkwijk M. H., Chang P., Justham S., 2010, [ApJ](#), **722**, L157

This paper was built using the Open Journal of Astrophysics L^AT_EX template. The OJA is a journal which

provides fast and easy peer review for new papers in the `astro-ph` section of the arXiv, making the reviewing process simpler for authors and referees alike. Learn more at <http://astro.theoj.org>.